ROYAL SOCIETY
OF CHEMISTRY

REVIEW

Check for updates

Minimizing energy losses in organic solar cells: mechanistic insights, material design, and morphological control

Zefeng Liu,[a] Jingming Xin,*[a] Xingpeng Liu,[a] Yutong Zhang,[a] Mingzhi Duan,[b] Yan Zhang,[a] Zhenhui Xu,[a] Junzheng Yan,[a] Qiuju Liang*[b] and Jiangang Liu [iD] *[a]

Organic solar cells (OSCs) exhibit promising potential for low-cost photovoltaic applications but suffer from high energy losses (E_{loss}) that critically limit their open-circuit voltage and power conversion efficiency. To address this challenge, this review first outlines the mechanistic origins of E_{loss}, emphasizing exciton dissociation barriers, charge-transfer state energetics, and recombination pathways, supported by quantitative characterization methodologies. Building on this foundation, material design strategies are analyzed, where molecular synthesis targeting backbone, side-chain, and terminal group optimization alongside ternary blending collectively modulates energy-level alignments to minimize driving-force offsets. Concurrently, morphological control approaches are systematically evaluated, demonstrating that precise regulation of phase separation, crystallinity, and molecular orientation effectively suppresses recombination losses and enhances charge transport. By integrating these advances, this work establishes a unified framework for energy loss minimization, providing critical insights for developing high-performance OSCs.

Broader context

Organic solar cells (OSCs) have garnered significant attentions as alternative photovoltaic technology due to inherent advantages. Substantial advances in organic semiconductors, morphology control, and interface engineering have elevated the power conversion efficiency (PCE) of OSCs to over 20%. Nevertheless, substantially higher energy loss compared to their inorganic counterparts consistently limits their performance, representing a critical challenge for further industrialization. This discrepancy is largely due to high energy loss (E_{loss}), which manifests primarily as a reduced open-circuit voltage (V_{OC}) and poses a major obstacle to commercialization. Reducing energy loss is therefore essential for enhancing device performance. This review comprehensively examines recent strategies aimed at mitigating energy loss in high-efficiency OSCs. We begin by outlining the fundamental mechanisms underlying energy loss and summarizing common characterization techniques. We then discuss material-based strategies-including molecular design and the incorporation of a third component-that optimize energy levels to increase V_{OC} and suppress energy loss. Furthermore, we explore morphology-centric approaches that reduce energy loss by enhancing charge transport and inhibiting bimolecular recombination, focusing on control of phase separation, crystallinity, and molecular orientation. By describing these developments, this review establishes design principles for minimizing energy loss and provides insightful perspectives toward achieving higher-performance OSCs.

1. Introduction

Organic solar cells (OSCs) present a promising pathway to address global energy crises and environmental degradation through photoelectric conversion.[1,2] Their inherent advantages, including lightweight construction,[3,4] economical fabrication,[5] and solution-processability, enable deployment in building-integrated systems[6,7] and portable electronics, thereby accelerating sustainable energy transitions. Driven by persistent materials synthesis and device engineering advances, bulk

heterojunction (BHJ) architectures[8,9] have become the dominant structure in OSCs, with single-junction devices now achieving power conversion efficiencies exceeding 20%.[9] Notably, blend systems incorporating high-performance polymer donors and non-fullerene acceptors simultaneously demonstrate exceptional metrics such as short-circuit current density ($J_{SC} > 25$ mA cm^{-2}), fill factor (FF > 80%), and external quantum efficiency (EQE > 85%)[10,11] comparable to perovskite and silicon-based solar cells. Nevertheless, OSC performance remains substantially inferior to that of perovskite (>26% PCE) and silicon solar cells (>27% PCE),[12,13] principally attributed to excessive energy loss (E_{loss}) manifested as reduced open-circuit voltage (V_{OC}). While silicon and perovskite devices exhibit E_{loss} values below 0.36 eV and 0.34 eV respectively,[14] state-of-the-art OSCs typically show $E_{loss} \approx 0.60$ eV,[15] significantly exceeding

[a]School of Electronics and Information, Northwestern Polytechnical University, Xi'an 710129, China. E-mail: jgliu@nwpu.edu.cn; xinjm@nwpu.edu.cn

[b]School of Microelectronics, Northwestern Polytechnical University, Xi'an 710129, China. E-mail: qiujuliang@nwpu.edu.cn

the Shockley–Queisser thermodynamic limit (0.25–0.30 eV).[16] Consequently, E_{loss} minimization is the critical performance constraint, positioning V_{OC} enhancement as the fundamental pathway for advancing OSC efficiencies.

Substantial energy loss in OSCs is attributed to their complex photoconversion mechanism. Characterized by low dielectric constants and strong electron-lattice coupling, organic semiconductors generate bounded electron–hole pairs called excitons with substantial coulombic binding energies (≈ 0.5 eV)[17,18] upon photoexcitation, instead of directly producing free charge carriers. The excitons diffuse to donor/acceptor (D/A) interfaces, undergoing conversion into charge-transfer (CT) states through energy-level offsets prior to dissociating into free carriers, a process that requires additional energy to overcome interfacial binding barriers.[19,20] Crucially, sub-bandgap absorption is induced by CT states, promoting radiative recombination and establishing the interfacial species as the primary contributors to energy loss. A critical inverse correlation is observed between the CT state energy (E_{CT}) and the magnitude of the D/A energy-level offsets: reduced offsets result in higher E_{CT} values.[21] Through strategic molecular engineering, E_{CT} can be systematically elevated to reduce sub-bandgap radiative recombination loss and associated energy dissipation. The energetic difference between the highest occupied molecular orbital (HOMO) of the donor and the lowest unoccupied molecular orbital (LUMO) of the acceptor is enlarged by diminished energy-level offsets,[22] thereby increasing V_{OC}. The optical bandgap (E_g) tuning in material systems further reduces energy loss in the device.

Precise energy-level modulation[23] and controlled morphology regulation[24] are the two primary strategies for mitigating energy loss in OSCs. Energy-level modulation, implemented through molecular synthesis or ternary strategies, reduces the donor HOMO level or elevates the acceptor LUMO level,[25,26] thereby enhancing V_{OC} and minimizing energy loss. For example, Li et al.[27] oxidized the dichloro terminal groups of BTP-eC9 to prepare BTP-eC9-4ClO, which increased the LUMO energy level of the acceptor and thus improved V_{OC}. Compared with the PM6:BTP-eC9 system, the PM6:BTP-eC9-4ClO system exhibited a decrease in ΔE_3 from 0.202 eV to 0.179 eV, a reduction in E_{loss} from 0.555 eV to 0.530 eV, an increase in V_{OC} from 0.861 V to 0.891 V, and an improvement in PCE from 19.12% to 20.03%. Concurrently, morphology regulation optimizes active layer nanostructures to achieve tailored phase separation, enhanced crystallinity, and favorable molecular orientation.[28,29] These structural features promote exciton dissociation and charge transport while suppressing bimolecular recombination. For instance, Zhang et al.[30] introduced donor D18-Cl and acceptor AITC into the D18:N3 system. D18-Cl acted as a nucleating agent promoting D18 aggregation, while AITC facilitated N3 aggregation, collectively enhancing crystallinity. Grazing incidence wide-angle X-ray scattering (GIWAXS) revealed an increased crystal coherence length (CCL) in the out-of-plane (010) direction (27.7 Å to 29.2 Å) for the D18:D18-Cl:N3:AITC film compared to D18:N3, indicating improved crystallinity that promoted charge transfer and suppressed recombination. Consequently, the D18:D18-Cl:N3:AITC device showed reduced ΔE_2 (0.060 eV to 0.050 eV), lower ΔE_3 (0.226 eV

to 0.216 eV), decreased E_{loss} (0.550 eV to 0.533 eV), increased V_{OC} (0.846 V to 0.869 V), and improved PCE (18.3% to 20.1%).

Given the critical role of minimizing energy loss in improving OSC performance, this review provides a systematic analysis of its underlying mechanisms and characterization techniques. Subsequently, we summarize material design strategies focused on energy-level modulation to reduce energy loss, including synthetic approaches for optimizing molecular backbones, side chains, and terminal groups.[31–33] Ternary strategies[34] are also covered, highlighting methods to elevate acceptor LUMO levels or lower donor HOMO levels, thereby increasing device V_{OC} and mitigating energy loss. Furthermore, we discuss morphology regulation as an effective pathway for energy loss reduction, analyzing control of phase separation, crystallinity, and molecular orientation to achieve optimal active layer structures[35,36] that suppress bimolecular recombination and enhance device performance. Finally, we present recent advancements and emerging research directions to deepen the fundamental understanding of energy loss processes, providing critical insights for future studies aimed at minimizing energy loss and advancing OSC technologies.

2. Energy loss mechanism and characterization

2.1 Energy loss mechanism

The efficient separation of photogenerated excitons into free charges at the D/A interface constitutes a critical process governing OSC performance.[37] Minimizing energy loss during this step while maintaining high charge generation efficiency is therefore essential. The E_{loss} in OSCs stems from the driving force required for exciton dissociation and non-radiative recombination phenomena.[38,39] Most organic semiconductors exhibit substantial coulombic exciton binding energies (≈ 0.5 eV), necessitating significant additional energy for charge dissociation in single-component systems. To circumvent this limitation, the BHJ structure is employed to construct a continuous nano-interpenetrating network within the active layer. This structure facilitates ultrafast exciton dissociation (<100 fs),[40] enabling high EQE and enhanced photocurrent generation. However, efficient charge dissociation and CT state formation mandate an optimal energy offset between the donor and acceptor materials. This energy offset is necessary to overcome the binding energy of interfacial CT excitons and dissociate them into free charges.[41,42] Consequently, optimizing the CT process to maximize extracted charge yield inherently involves energy loss. Moreover, disordered molecular packing[43] within the OSC active layer further contributes substantially to non-radiative energy loss.

Generally, E_{loss} is typically defined relative to the CT state (Fig. 1A). It comprises two components: energy loss during free charge generation (ΔE_2) and energy loss from free charge recombination ($E_{CT} - qV_{OC}$). Furthermore, the recombination loss is further subdivided into radiative (ΔE_1) and non-radiative (ΔE_3) components. ΔE_1 originates from the mismatch between solar radiation and absorbed omnidirectional blackbody
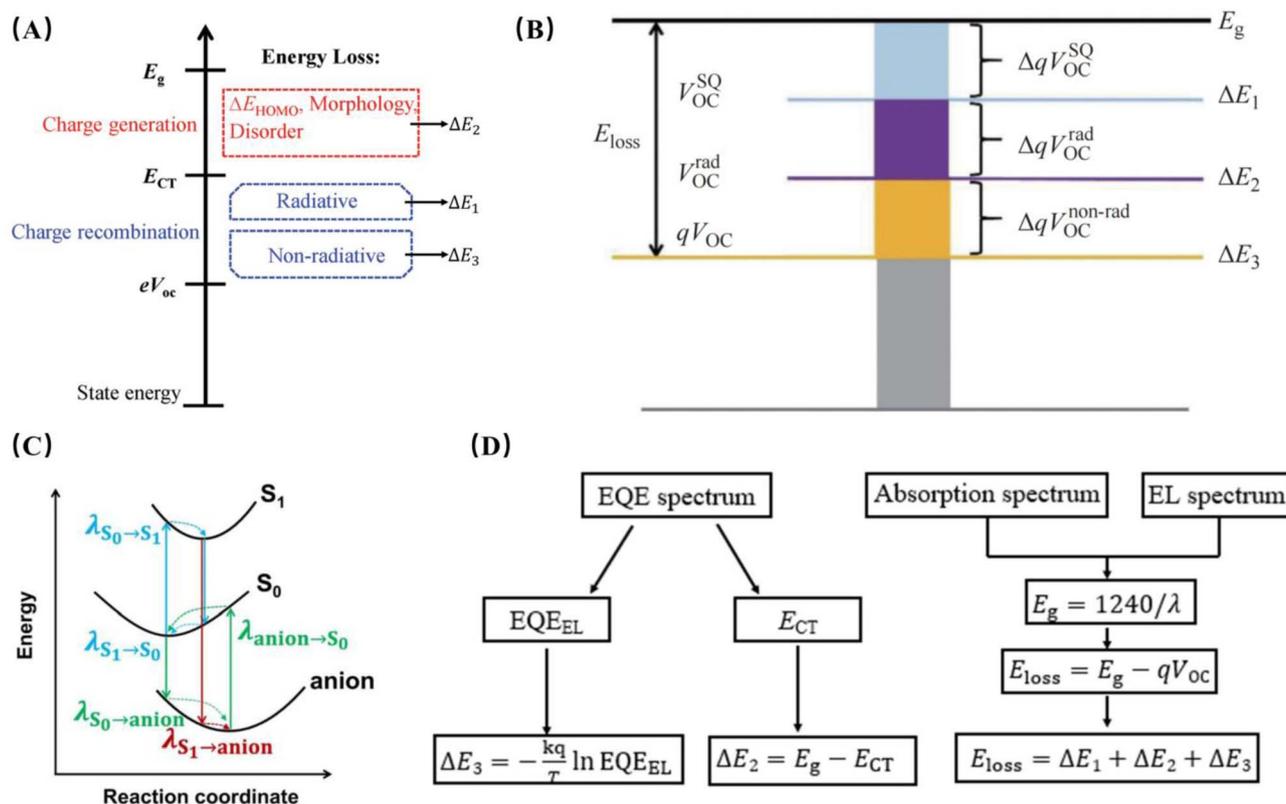
Fig. 1 (A) Pathways of energy loss in OSCs bounded by the energy of the CT state; (B) schematic illustration of energy loss in OSCs based on the SQ theory; (C) correlated transition processes between the ground state (S_0), singlet excited state (S_1), and anion state; (D) energy loss calculation flowchart.

radiation above E_g which is inevitable for any OSC once E_g is fixed. ΔE_2 is closely related to $\Delta E_{LE–CT}$ (the energy difference between the localized excitonic state and the CT state). An increase in $\Delta E_{LE–CT}$ indicates a larger energy offset between the donor and acceptor, corresponding to a stronger driving force for exciton dissociation. In previous studies, it was generally believed that efficient exciton dissociation in OSCs requires a considerable driving force (>0.3 eV),[44,45] leading to a large ΔE_2. Currently, ΔE_2 can be reduced by continuously decreasing the energy offset between the donor and acceptor materials. ΔE_3 is caused by non-radiative recombination at the D/A interface in OSCs, with this energy loss being exclusively determined by the device's EQE_{EL} (electroluminescence quantum efficiency of the solar cell upon carrier injection under dark conditions). The value of ΔE_3 typically ranges from 0.20 eV to 0.30 eV,[46,47] and it is difficult to keep ΔE_3 at a low level. As consistent with the above, ΔE_3 has become the main limiting factor affecting the total E_{loss}. Consequently, reduction of non-radiative energy loss is essential for enhancing the power conversion efficiency in OSCs.

2.2 Characterization methods

Despite the persistent challenge of accurately quantifying CT state energies, significant efforts have been directed toward developing simplified computational models to reliably estimate E_{loss} in OSCs. As illustrated in Fig. 1B and defined by the SQ limit framework, the E_{loss} in OSCs is partitioned into three distinct components via a specific formula.

$$E_{loss} = q\Delta V_{OC} = E_g - qV_{OC}$$
$$= (E_g - qV_{OC}^{SQ}) + (qV_{OC}^{SQ} - qV_{OC}^{rad}) + (qV_{OC}^{rad} - qV_{OC})$$
$$= (E_g - qV_{OC}^{SQ}) + q\Delta V_{OC}^{rad,below\ gap} + q\Delta V_{OC}^{non-rad}$$
$$= \Delta E_1 + \Delta E_2 + \Delta E_3$$

Herein, E_g is the optical band gap, V_{OC}^{SQ} is the maximum voltage based on the SQ limit, V_{OC}^{rad} is the open-circuit voltage with only radiative recombination, $\Delta V_{OC}^{rad,below\ gap}$ is the voltage loss caused by radiative recombination below the band gap, and $\Delta V_{OC}^{non-rad}$ is the voltage loss caused by non-radiative recombination. While this calculation method parallels the aforementioned approach bounded by E_{CT}, the energy loss ΔE_1 and ΔE_2 exhibit distinct origins, where ΔE_1 quantifies unavoidable radiative recombination loss above the bandgap, with a typical value of approximately 0.30 eV; ΔE_2 originates from radiative recombination loss below the bandgap, generally ranging between 0.02 and 0.08 eV;[48,49] ΔE_3, which corresponds directly to its counterpart in the previous method and is calculated as $-kT/q \ln(EQE_{EL})$, stems from non-radiative recombination. The value of ΔE_3 typically falls within 0.20–0.30 eV (ref. 50 and 51) and proves difficult to minimize. Consequently, ΔE_3 constitutes the primary limiting factor governing E_{loss} and further impacting the PCE of OSCs through maximizing V_{OC} (or minimizing voltage loss to the greatest extent) without sacrificing J_{SC} and FF.[52,53]

To precisely characterize energy loss, the absorption spectrum of the active layer first corresponds to the photon energy
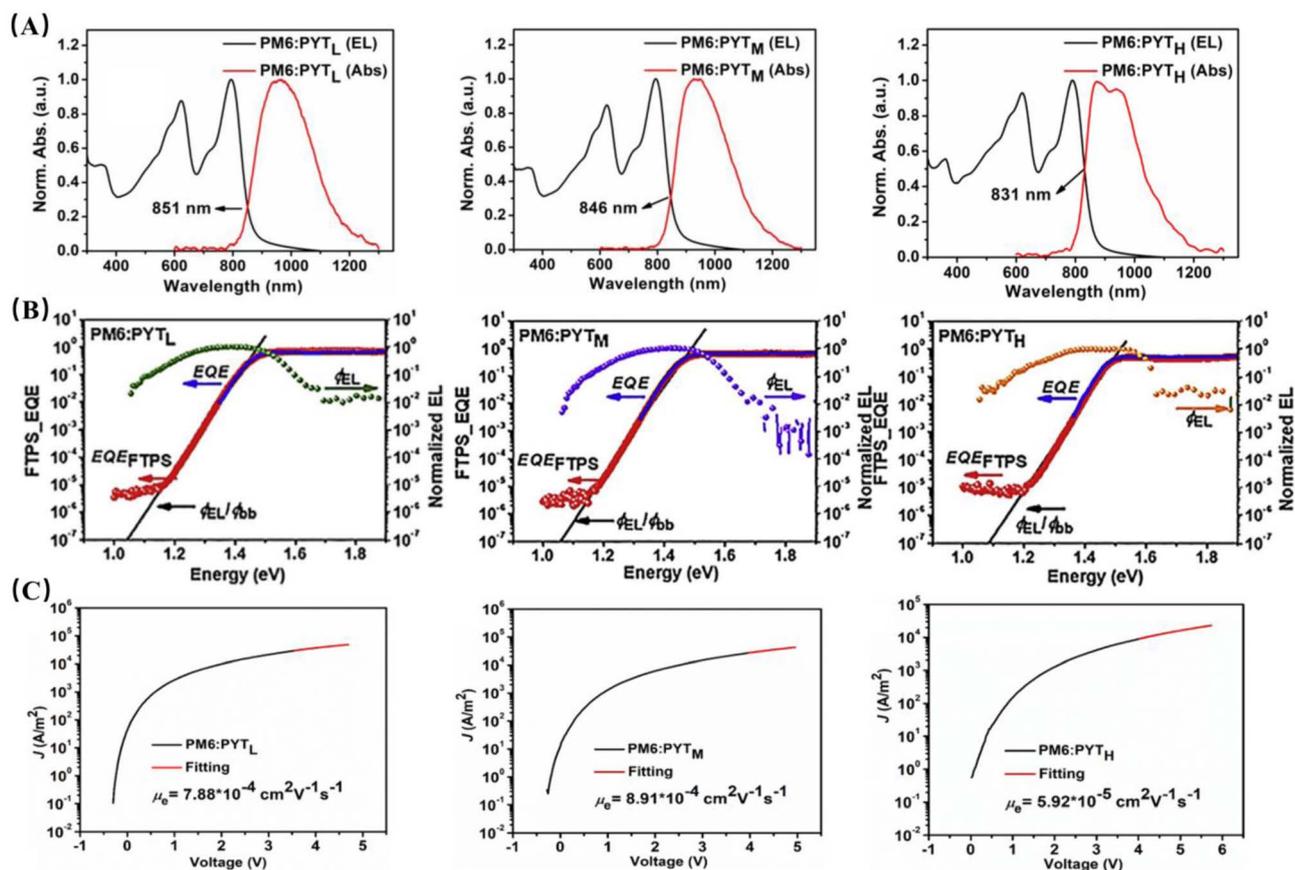
Fig. 2 (A) Normalized absorption and EL spectra of PM6:PYT$_L$, PM6:PYT$_M$ and PM6:PYT$_H$ blends; (B) semi-logarithmic plots display the normalized electroluminescence (EL), the measured external quantum efficiency (EQE), and the EQE derived from Fourier-transform photo-current spectroscopy (EQE$_{FTPS}$) as functions of photon energy for devices based on PM6:PYT$_L$, PM6:PYT$_M$, and PM6:PYT$_H$; (C) the dark J–V characteristics of PM6:PYT$_L$, PM6:PYT$_M$, and PM6:PYT$_H$ based electron-only devices. The red lines represent the best fitting using the SCLC model.[60] Copyright 2020 Elsevier.

absorbed during transitions from the ground state (S$_0$) to the first excited state (S$_1$),[54,55] as depicted in Fig. 1C. The long-wavelength absorption edge (absorption cutoff) corresponds to the E_g, representing the minimum energy required to excite an electron from the valence band maximum to the conduction band minimum. The electroluminescence (EL) spectrum arises from photon emission during exciton recombination.[56,57] In OSCs, it predominantly corresponds to radiative recombination of CT charges or excitons within the active layer, where the EL peak energy consistently lies below the material's E_g due to energy loss. Significantly, the energy at which the absorption and EL spectra intersect simultaneously satisfies the minimum energy for exciton generation (absorption cutoff) and the maximum energy for radiative recombination (high-energy EL emission limit).[58,59] This intersection energy therefore equates to the material's E_g, quantifying the energy difference between the ground-state and excited-state excitonic configurations. Furthermore, E_{loss} and ΔE_1, ΔE_2, and ΔE_3 can be determined according to the SQ limit (Fig. 1D).

The E_g of the active layer was determined from the inter-section point between the device's EL spectrum and the absorption spectrum of the active layer film. Device E_{loss} is quantified using the V_{OC} and E_g. Through computational deconvolution according to the SQ framework, E_{loss} partitions into three discrete components, enabling precise determination of ΔE_1, ΔE_2 and ΔE_3 values. Following this method, Min et al.[60] calculated E_g based on the intersection of the EL spectrum and absorption spectrum ($E_g = 1240/\lambda$), obtaining E_g values of 1.457 eV, 1.466 eV, and 1.492 eV for the PM6:PYT$_L$, PM6:PYT$_M$, and PM6:PYT$_H$ blends (Fig. 2A). Subsequently, using the E_g values, the E_{loss} for each corresponding device was calculated, yielding loss values of 0.532 eV, 0.528 eV, and 0.544 eV, respectively. For PM6:PYT$_L$, $\Delta E_1 = 0.258$ eV, $\Delta E_2 = 0.045$ eV, $\Delta E_3 = 0.229$ eV; for PM6:PYT$_M$, $\Delta E_1 = 0.259$ eV, $\Delta E_2 = 0.058$ eV, and $\Delta E_3 = 0.210$ eV; for PM6:PYT$_H$, $\Delta E_1 = 0.260$ eV, $\Delta E_2 = 0.062$ eV, and $\Delta E_3 = 0.222$ eV (Fig. 2B). This comprehensive approach combining electroluminescence and absorption spectroscopy thus provides a quantitative method for evaluating and understanding the energy loss mechanisms in the device. The hole and electron mobilities (μ_h/μ_e) of the PM6:PYT$_L$, PM6:PYT$_M$, and PM6:PYT$_H$ blends were determined by SCLC measurements to be $2.81 \times 10^{-4}/7.88 \times 10^{-4}$ cm^2 V^{-1} s^{-1}, $6.12 \times 10^{-4}/8.91 \times 10^{-4}$ cm^2 V^{-1} s^{-1}, and $0.249 \times 10^{-4}/0.592 \times 10^{-4}$ cm^2 V^{-1} s^{-1} (Fig. 2C), respectively. Among them, the PM6:PYT$_M$-based

device exhibits the highest and most balanced charge carrier mobility, which is advantageous for efficient charge transport.

3. Material and component adjustment

The V_{OC} in OSCs scales directly with the donor–acceptor energy difference between the donor's HOMO and the acceptor's LUMO, governing V_{OC} while controlling charge-transfer driving forces. Consequently, targeted energy-level modulation enhances V_{OC} while E_g alignment reduces energy loss, collectively advancing device performance metrics. This section outlines molecular synthesis approaches and ternary strategies[61,62] to systematically modulate the energy levels of the donor and acceptor for lowering energy loss.[11,63]

3.1 Molecular synthesis strategy

Molecular synthesis strategies enable precise energy-level modification in both donor and acceptor materials through targeted structural modifications across three key dimensions: backbone engineering, side-chain engineering, and terminal

group modification.[64,65] The modifications regulate material energy levels to minimize donor–acceptor energy offsets, thereby elevating the CT state energy and reducing energy loss. The fundamental principle centers on optimized energy level alignment, which simultaneously ensures sufficient exciton dissociation driving force while maximizing the theoretical V_{OC} limit, ultimately minimizing energy loss.[19,66]

3.1.1 Molecular backbone. Optimization of donor–acceptor energy level alignment is achieved through molecular chain structure modification or polymer backbone molecular weight control.[67,68] An optimal energy level offset enables efficient interfacial exciton dissociation into free charges. This provides sufficient thermodynamic driving force while simultaneously minimizing charge recombination energy loss. For example, precise molecular weight adjustment optimizes material energy levels and interfacial offsets to achieve enhanced V_{OC} and reduced energy loss. He et al.[69] designed donors with varied molecular weights (Fig. 3A). Compared to PBD-Cl$_H$ ($M_n = 76.2$ kDa), PBD-Cl$_M$ ($M_n = 60.3$ kDa) exhibited a decreased HOMO level (-5.48 eV to -5.52 eV). Consequently, the PBD-Cl$_M$:N3 device showed reduced ΔE_3 (0.260 eV to 0.252 eV), increased V_{OC} (0.84 V to 0.86 V), and improved PCE (9.00% to 17.17%) versus
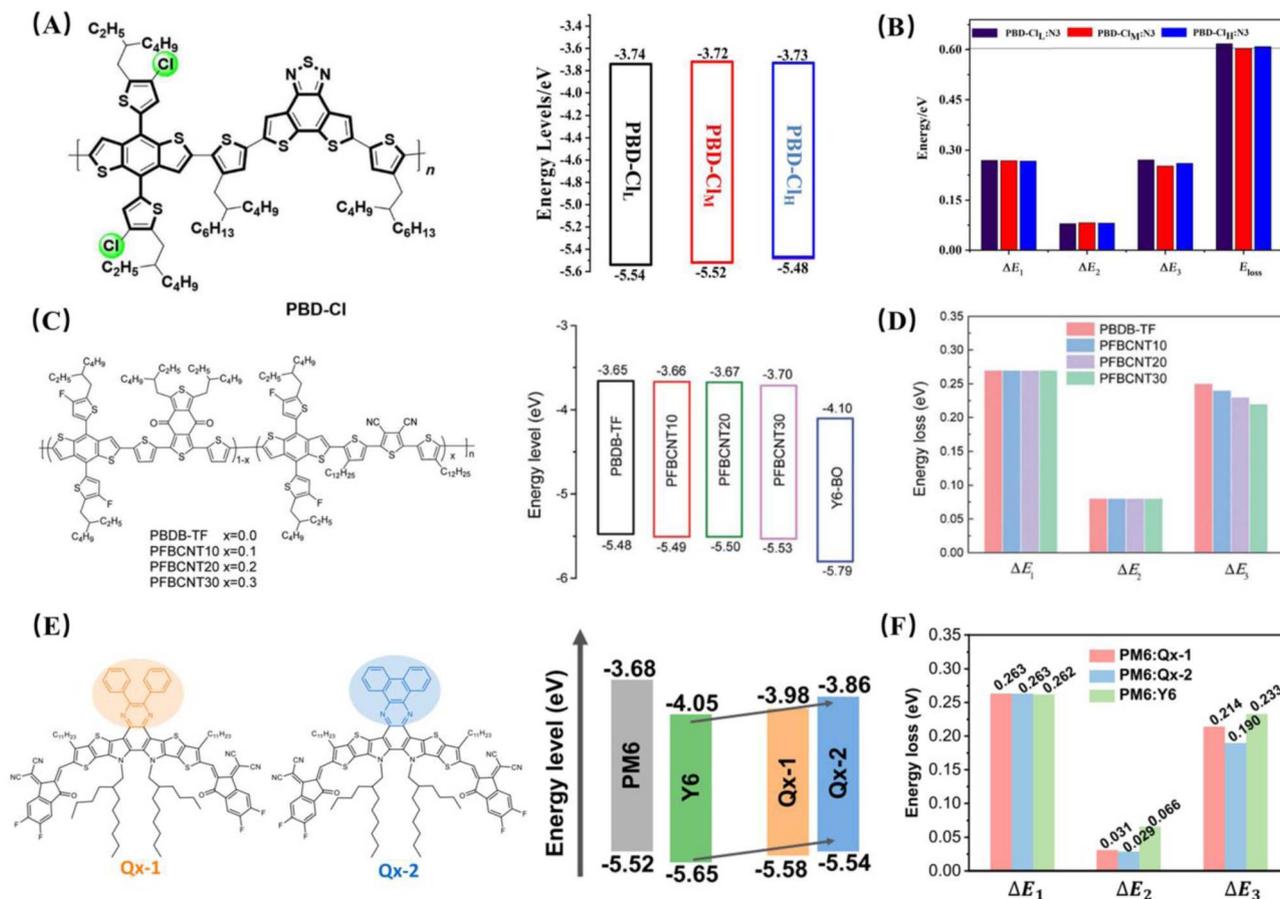

Fig. 3 (A) Chemical structure and energy level of PBD-Cl; (B) energy loss of devices based on PBD-Cl$_L$:N3, PBD-Cl$_M$:N3, and PBD-Cl$_H$:N3.[69] Copyright 2024 WILEY-VCH. (C) Structure diagram of PFBCNTx and energy level of donor–acceptor materials; (D) energy loss of devices based on PBDB-TF and PFBCNTx.[72] Copyright 2021 The Royal Society of Chemistry. (E) Chemical structures and energy levels of Qx-1 and Qx-2; (F) energy loss of binary OSC devices based on Qx-1 and Qx-2.[73] Copyright 2022 Springer Nature.

PBD-Cl$_H$:N3 (Fig. 3B). In addition, modifying the molecular backbone structure can also tune material energy levels.[70,71] Duan et al.[72] incorporated DCT units into PBDB-TF, synthesizing PFBCNTx donors with controlled weights: PBDB-TF (M_n = 36.0 kDa), PFBCNT10 (M_n = 43.3 kDa), and PFBCNT20 (M_n = 49.5 kDa) (Fig. 3C). Importantly, DCT molecular weight adjustment stabilized E_g but decreased the donor HOMO level (−5.48 eV to −5.50 eV). This enlarged donor HOMO-acceptor LUMO energy difference promotes charge transfer, enhancing V_{OC}. Ultimately, the PFBCNT20:Y6-BO device demonstrated reduced ΔE_3 (0.25 eV to 0.23 eV), lower E_{loss} (0.60 eV to 0.58 eV), increased V_{OC} (0.81 V to 0.85 V), and higher PCE (15.7% to 16.6%) (Fig. 3D).

Molecular backbone modification through the introduction of electron-withdrawing groups enables alteration of molecular electron cloud distribution[74,75] which can achieve optimized donor–acceptor alignment. This facilitates interfacial charge transfer while reducing charge transport energy loss. For example, Wei et al.[73] synthesized acceptors Qx-1 and Qx-2 by fusing Qx derivatives into Y-series backbones (Fig. 3E). Replacing Y6's BTZ core with the more electron-withdrawing Qx core weakened intramolecular charge transfer (ICT), elevating the acceptor LUMO level from −4.05 eV (Y6) to −3.86 eV. According to space charge limited current (SCLC) measurements, the hole and electron mobilities (μ_h and μ_e) of the PM6:Qx-1 blend film were determined to be 3.64×10^{-4} cm^2 V^{-1} s^{-1} and 1.88×10^{-4} cm^2 V^{-1} s^{-1}, respectively. In comparison, the PM6:Y6 blend film exhibited μ_h and μ_e values of 3.36×10^{-4} cm^2 V^{-1} s^{-1} and 1.33×10^{-4} cm^2 V^{-1} s^{-1}, respectively. The PM6:Qx-1 blend demonstrates a more balanced charge carrier mobility compared to PM6:Y6, which is beneficial for enhanced charge transport properties. Consequently, the PM6:Qx-1 device exhibited reduced ΔE_2 (0.066 eV to 0.031 eV), lower ΔE_3 (0.233 eV to 0.214 eV), decreased E_{loss} (0.561 eV to 0.508 eV), increased V_{OC} (0.859 V to 0.911 V), and higher PCE (16.6% to 17.9%) versus PM6:Y6 (Fig. 3F). Alex K.-Y. Jen et al.[76] introduced selenium (Se) atoms into PYT-2S to prepare PYT-1S1Se and PYT-2Se (Fig. 4A). Increased Se content lowered acceptor LUMO levels. PYT-1S1Se exhibited a higher LUMO level (−3.75 eV) than PYT-2Se (−3.79 eV). The PM6:PYT-1S1Se device thus showed reduced ΔE_2 (0.042 eV to 0.037 eV), lower E_{loss} (0.510 eV to 0.506 eV), increased V_{OC} (0.908 V to 0.926 V), and improved PCE (15.5% to 16.3%) relative to PM6:PYT-2Se (Fig. 4B). Notably, Sun et al.[77] further demonstrated this approach by introducing T-F units into PTQ10, yielding PTQ13-5 (Fig. 4C). The strong electron-withdrawing nature of fluorine atoms decreased the donor HOMO level from −5.51 eV to −5.54 eV. SCLC measurements were further conducted on PTQ13-5:K4 and PTQ10:K4 devices, revealing hole and electron mobilities (μ_h and μ_e) of 6.89×10^{-4}/7.13×10^{-4} cm^2 V^{-1} s^{-1} and 5.98×10^{-4}/6.54×10^{-4} cm^2 V^{-1} s^{-1}, respectively. The corresponding μ_h/μ_e ratios were calculated to be 0.96 and 0.91. The PTQ13-5:K4-based device exhibits higher μ_h and μ_e values along with a more balanced charge transport ratio, leading to improved charge carrier extraction and overall device performance. The PTQ13-5:K4 device consequently demonstrated reduced ΔE_3 (0.207 eV to 0.189 eV), lower E_{loss} (0.514 eV to 0.506 eV), increased V_{OC}

(0.888 V to 0.891 V), and higher PCE (17.61% to 18.42%) versus PTQ10:K4 (Fig. 4D).

Optimization of molecular backbone geometry enhances structural regularity and enables precise energy level alignment in donor–acceptor systems.[78,79] This modification promotes improved orbital overlap between adjacent molecules, facilitating the formation of continuous charge transport pathways. Consequently, carrier recombination during transport is suppressed, leading to minimized energy loss. For example, Li et al.[80] developed alkyne-linked oligomeric electron acceptors (S-Alkyne-YF and T-Alkyne-YF) derived from M3 (Fig. 4E). Alkyne linkages, with their high bond dissociation energies and planar geometries, boost molecular planarity and promote ordered aggregation in thin films. Compared to S-Alkyne-YF, T-Alkyne-YF shows a higher peak (I_{0-0}/I_{0-1}) ratio, indicating stronger molecular aggregation and better packing order. It also exhibits a slightly raised LUMO energy level (−3.82 eV to −3.79 eV), widening the energy level offset for increased V_{OC} and reduced energy loss. As shown in Fig. 4F, the PM6:T-Alkyne-YF device (vs. PM6:S-Alkyne-YF) shows lower ΔE_3 (0.218 eV to 0.185 eV) and E_{loss} (0.536 eV to 0.516 eV), higher V_{OC} (0.894 V to 0.943 V), and improved PCE (13.96% to 17.90%). Bo et al.[81] synthesized polymer donor PL1 via random copolymerization of PM6 and D18 units (Fig. 4G). This reduced the HOMO level from −5.51 eV to −5.55 eV (Fig. 4H), reducing the energy level offset. SCLC measurements revealed hole and electron mobilities (μ_h and μ_e) of 8.87×10^{-4}/7.45×10^{-4} cm^2 V^{-1} s^{-1} for the PL1:BTP-eC9-4F device and 6.97×10^{-4}/6.04×10^{-4} cm^2 V^{-1} s^{-1} for the D18:BTP-eC9-4F device. The higher and more balanced charge carrier mobilities observed in the PL1-based blend contribute to enhanced charge transport properties. The PL1:BTP-eC9-4F device thus showed reduced ΔE_3 (0.260 eV to 0.185 eV), lower E_{loss} (0.583 eV to 0.535 eV), increased V_{OC} (0.827 V to 0.876 V), and improved PCE (16.18% to 18.14%) relative to D18:BTP-eC9-4F.

3.1.2 Molecular side chains. Molecular side chains are modulated through halogen atom incorporation or alkyl chain tailoring,[82,83] altering electron cloud distribution along conjugated backbones. This redistribution shifts molecular HOMO and LUMO energy levels,[84,85] promoting optimized donor–acceptor alignment. Consequently, enhanced charge transport, improved collection efficiency, and suppressed non-radiative recombination are achieved, collectively reducing energy loss. For example, halogenation of side chains enables precise energy level optimization that minimizes donor–acceptor energy level offsets, consequently enhancing device V_{OC} while reducing energy loss and collectively improving photovoltaic performance. Chen et al.[86] chlorinated PBDTSi-TZ to yield PBDTCl-TZ (Fig. 5A), reducing the donor HOMO level from −5.38 eV to −5.48 eV (Fig. 5B). Relative to the PBDTSi-TZ:IT-4F device, the PBDTCl-TZ:IT-4F system demonstrated significant performance enhancements including reduced ΔE_3 (0.405 eV to 0.361 eV), lower E_{loss} (0.790 eV to 0.715 eV), increased V_{OC} (0.781 V to 0.837 V), and enhanced PCE (11.26% to 12.21%). Similarly, Zhou et al.[87] synthesized a donor PE62 and an acceptor F-Qx3b as shown in Fig. 5C. Site-specific fluorination lowered the donor HOMO level from −5.19 eV to −5.37 eV (Fig. 5D), expanding the
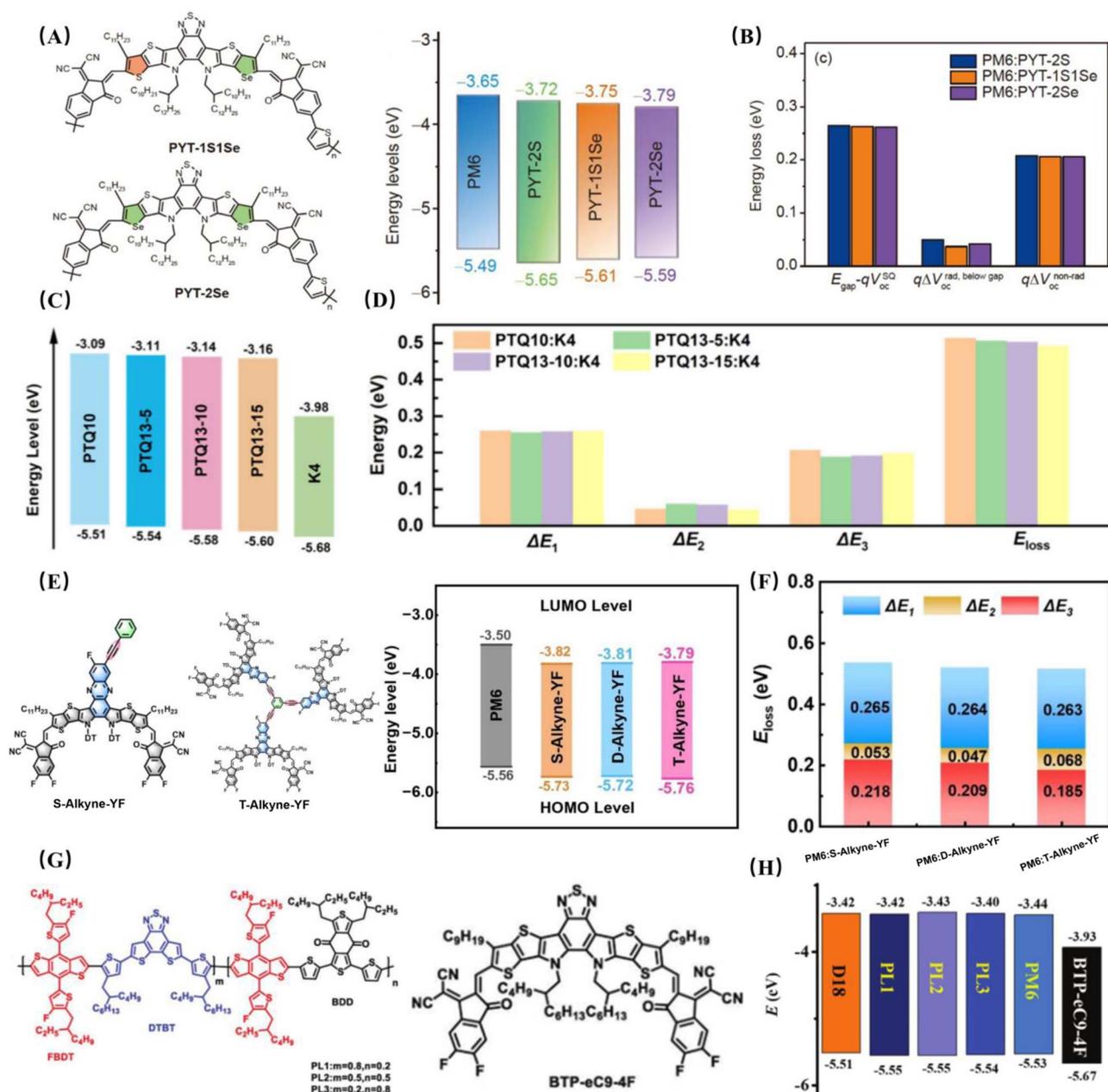
Fig. 4 (A) Chemical structures and energy levels of PYT-1S1Se and PYT-2Se; (B) energy loss of devices based on PM6:PYT-1S1Se and PM6:PYT-2Se.[76] Copyright 2021 Springer Nature. (C) Energy levels of PTQ10 and PTQ13-5; (D) energy loss of devices based on PTQ10:K4 and PTQ10:K4.[77] Copyright 2025 American Chemical Society. (E) Chemical structures and energy levels of S-Alkyne-YF and T-Alkyne-Y; (F) energy loss of devices based on PM6:S-Alkyne-YF and PM6:T-Alkyne-Y.[80] Copyright 2025 WILEY-VCH. (G) Chemical structures of PL1, PL2, PL3, and BTP-eC9-4F; (H) energy levels of PL1, PL2, PL3, and BTP-eC9-4F.[81] Copyright 2022 WILEY-VCH.

energy offset. SCLC measurements were carried out to evaluate the hole and electron mobilities (μ_h and μ_e) of the PE61:Qx3b and PE62:F-Qx3b devices, yielding values of $2.86 \times 10^{-4}/8.38 \times 10^{-4}$ cm^2 V^{-1} s^{-1} and $8.69 \times 10^{-4}/5.07 \times 10^{-4}$ cm^2 V^{-1} s^{-1}, respectively. The PE62:F-Qx3b-based device exhibits higher charge carrier mobilities and a more balanced μ_h/μ_e ratio, which contributes to improved charge transport characteristics. The PE62:F-Qx3b device consequently achieved reduced E_{loss} (0.67 eV to 0.61 eV), higher V_{OC} (1.02 V to 1.09 V), and improved

PCE (8.24% to 9.78%). MAL2-sCl, a chlorinated-side-chain acceptor synthesized by Gao et al.,[67] displayed an elevated LUMO energy level of −3.87 eV compared to MAL1 (−3.89 eV). The PM7:MAL2-sCl device showed diminished ΔE_3 (0.31 eV to 0.26 eV), reduced E_{loss} (0.80 eV to 0.73 eV), elevated V_{OC} (0.996 V to 1.000 V), and substantially higher PCE (4.37% to 5.75%) with the performance improved by nearly 30%.

Tailoring alkyl side chains effectively optimizes material energy levels and modulates donor–acceptor offsets.[88–90] This
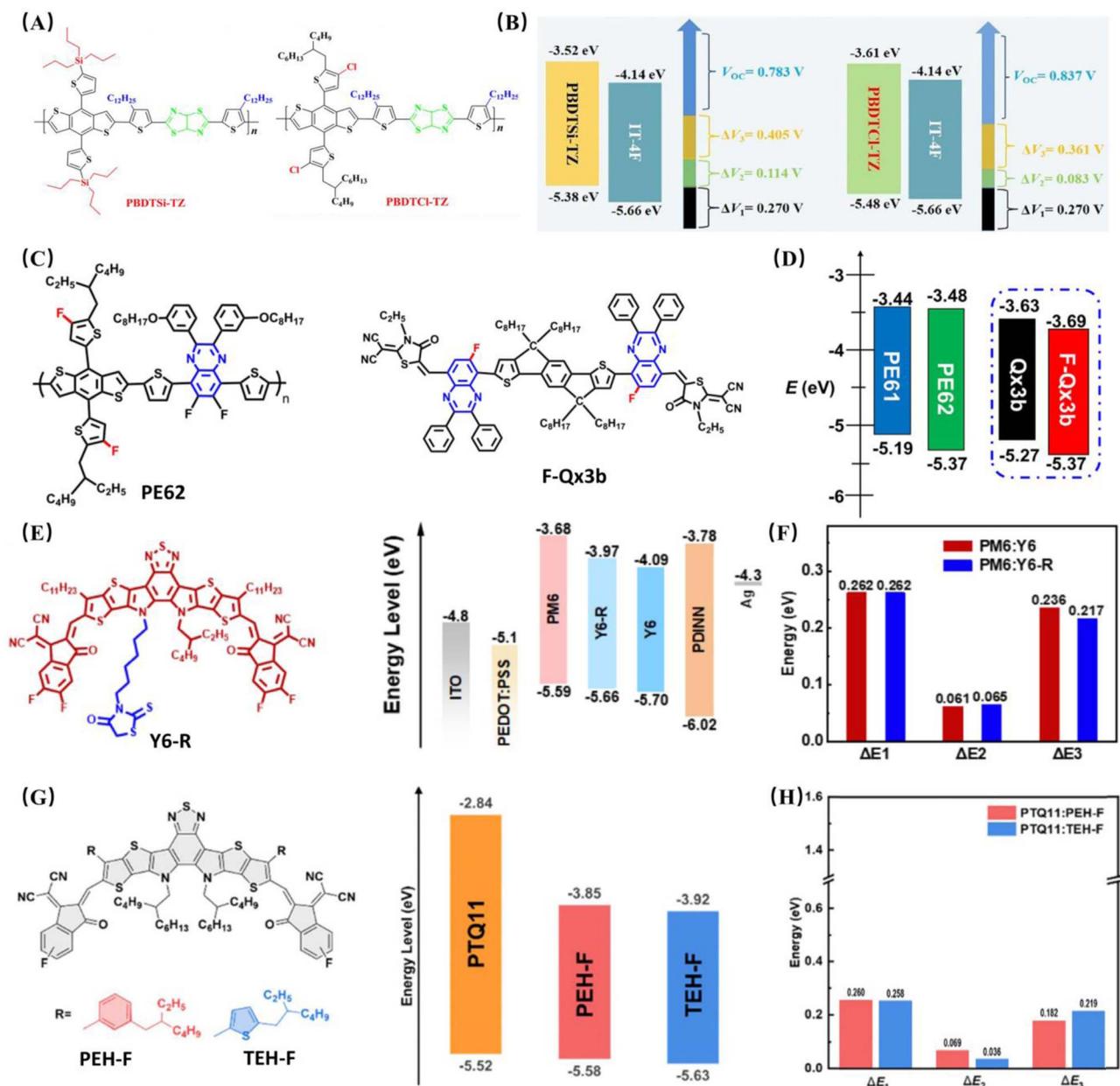
Fig. 5 (A) Chemical structures of PBDTSi-TZ and PBDTCl-TZ; (B) energy loss of devices based on PBDTSi-TZ:IT-4F and PBDTCl-TZ:IT-4F.[86] Copyright 2020 WILEY-VCH. (C) Chemical structures of PE62 and F-Qx3b; (D) energy levels of PE62 and F-Qx3b.[87] Copyright 2021 Elsevier. (E) Chemical structure of Y6-R and energy level of its device; (F) energy loss of devices based on PM6:Y6 and PM6:Y6-R.[91] Copyright 2025 American Chemical Society. (G) Chemical structures and energy levels of PEH-F and THE-F; (H) energy loss of devices based on PTQ11:PEH-F and PTQ11:THE-F.[92] Copyright 2025 Royal Society of Chemistry.

molecular engineering approach facilitates elevated V_{OC}, mitigated energy loss, and enhanced photovoltaic device performance. For instance, an asymmetric small-molecule acceptor, Y6-R, was developed by Zhou et al.[91] (Fig. 5E). Its LUMO energy level increased from −4.09 eV to −3.97 eV compared to Y6. Relative to the PM6:Y6 device (Fig. 5F), the PM6:Y6-R counterpart demonstrated a reduction in ΔE_3 (0.236 eV to 0.217 eV), lower E_{loss} (0.559 eV to 0.544 eV), higher V_{OC} (0.839 V to 0.863 V), and an improved PCE (16.84% to 18.62%). Similarly, Sun et al.[92] designed and synthesized two acceptors, PEH-F and

TEH-F, with different conjugated outer side chains (Fig. 5G). The LUMO energy level of the acceptor increased from −3.92 eV to −3.85 eV. Compared with the PTQ11:TEH-F device (Fig. 5H), the PTQ11:PHE-F-based device showed a decrease in ΔE_3 from 0.219 eV to 0.182 eV, an increase in V_{OC} from 0.909 V to 0.936 V, and an improvement in PCE from 17.40% to 19.73%. Chen et al.[93] employed an asymmetric design to develop acceptor BTP-BO-TBO, featuring alkyl/thienyl hybrid side chains. Its LUMO level increased from −3.99 eV to −3.91 eV compared to BTP-DTBO, enlarging the energy level offset and boosting V_{OC}. The

PM6:BTP-BO-TBO device showed reductions in ΔE_2 (0.055 eV to 0.027 eV), ΔE_3 (0.233 eV to 0.198 eV), and E_{loss} (0.550 eV to 0.485 eV), alongside increased V_{OC} (0.878 V to 0.907 V) and PCE (17.22% to 19.76%).

3.1.3 Terminal groups. Modification of terminal groups[94,95] provides a straightforward strategy for precise molecular energy-level modulation. This approach enables optimization of HOMO and LUMO energy levels through tailored electronic properties leading to enhanced donor–acceptor energy level offsets, reduced E_{loss} in charge transfer states, and ultimately improved charge transport and collection. For example, BTP-FT (Fig. 6A) was synthesized through introducing a fluorinated thiophene-extended terminal group (IC-FT) into BTP-4F by Wang et al.[96] Relative to BTP-4F, an upshifted LUMO level was observed in BTP-FT (−4.17 eV vs. −4.23 eV). This modification enlarged the energy level offset and promoted charge transfer. The corresponding PM6:BTP-FT device (Fig. 6B) demonstrated reduced ΔE_2 (0.053 eV vs. 0.066 eV), ΔE_3 (0.203 eV vs. 0.254 eV), and E_{loss} (0.523 eV vs. 0.585 eV), alongside increased V_{OC}

(0.900 V vs. 0.812 V) and PCE (17.56% vs. 14.90%) compared to PM6:BTP-4F. Wei et al.[97] synthesized BTP-C9-ICT via π-extension of Y5 with thiophene groups (Fig. 6C). The modified acceptor exhibited an elevated HOMO level (−3.89 eV vs. −3.96 eV), enhancing V_{OC}. The corresponding device (Fig. 6D) showed reduced ΔE_3 (0.15 eV vs. 0.18 eV), lower E_{loss} (0.49 eV vs. 0.52 eV), increased V_{OC} (0.99 V vs. 0.95 V), and improved PCE (11.42% vs. 7.56%) relative to PM6:Y5. The A–D–A type acceptor CH17 was constructed based on Y6, featuring prominent π-extension (Fig. 6E) by Chen et al.[98] A marginally increased LUMO level (−3.86 eV vs. −3.87 eV) was observed. The extended conjugation enhanced intermolecular interactions and molecular packing order (Fig. 6F), yielding a device with reduced ΔE_3 (0.19 eV vs. 0.24 eV), lower E_{loss} (0.50 eV vs. 0.53 eV), higher V_{OC} (0.883 V vs. 0.852 V), and improved PCE (17.84% vs. 16.27%).

3.1.4 Bridging core. Modifying the bridging core within conjugated molecular architectures serves as an effective strategy to fine-tune the conjugation length and electronic properties of organic photovoltaic materials. By systematically
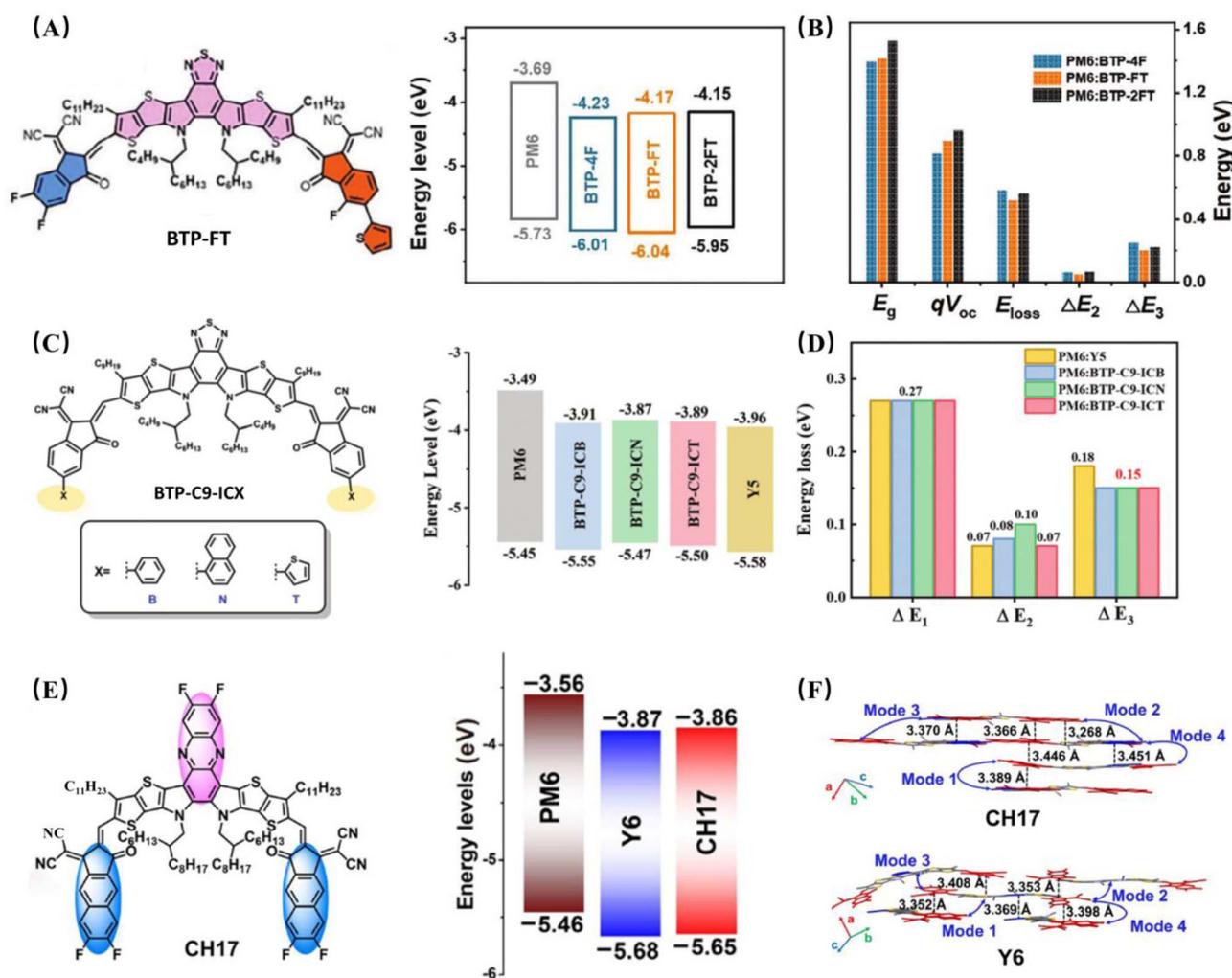

Fig. 6 (A) Chemical structure and energy level of BPT-FT; (B) energy loss of devices based on PM6:BPT-4F and PM6:BPT-FT.[96] Copyright 2025 WILEY-VCH. (C) Chemical structure and energy level of BTP-C9-ICX; (D) energy loss of devices based on PM6:Y5 and PM6:BTP-C9-ICT.[97] Copyright 2022 Royal Society of Chemistry. (E) Chemical structure and energy level of CH17; (F) π−π stacking distances between molecular layers and different molecular packing modes of CH17 and Y6.[98] Copyright 2022 Springer Nature.

altering the chemical structure and electronic nature of the bridge, researchers can modulate the bandgap and energy levels of the resulting material with precision. Such control enables an optimized alignment between the donor and acceptor energy levels, which facilitates more efficient charge transfer and reduces the energy offset required for charge separation. As a result, voltage loss-particularly non-radiative recombination loss-is significantly suppressed, leading to higher open-circuit voltage and improved overall device performance. This molecular-level engineering underscores the critical role of the bridging unit in minimizing energy loss and enhancing the efficiency of organic solar cells. By modulating the position and number of π-bridges in the side chains, Song et al.[99] synthesized two acceptors, 2T-T-EH and 2T-TT-2EH. Compared to 2T-T-EH, 2T-TT-2EH exhibits a raised LUMO energy level from −3.87 eV to −3.81 eV. In devices based on JD40:2T-TT-2EH, this modification resulted in a reduction of the ΔE_{nr} from 0.342 eV to 0.303 eV and a decrease in the E_{loss} from 0.688 eV to 0.629 eV, accompanied by an increase in V_{OC} from 0.825 V to 0.916 V and an improvement in PCE from 13.44% to 14.17%. He et al.[100] developed a bridged acceptor, DY-FL, through strategic modification of the linkage site and connecting unit based on the Y-F structure. This molecular design enables the LOMO energy level to reach −3.87 eV, which is higher than the −3.90 eV of the parent Y-F molecule, leading to an enhanced V_{OC} and reduced energy loss in the corresponding devices. When blended with PM6, the DY-FL-based device exhibited a reduced energy loss term ΔE_3 of 0.24 eV, down from 0.25 eV in the PM6:Y-F device, along with an improved VOC of 0.890 V (versus 0.861 V) and a higher power conversion efficiency (PCE) of 19.78% compared to 17.53%.

3.2 Ternary strategy

In traditional binary blend systems, incorporating a third component mitigates energy loss pathways while simultaneously broadening the absorption spectral range.[101,102] Rational selection of the third component enables precise tuning of the donor and acceptor energy levels. This optimization enhances the V_{OC}, reducing energy loss for improved overall device performance.

Strategic incorporation of a third component with strong D/A interactions facilitates the formation of an alloy phase[103,104] that enables precise energy-level and E_{CT} modulation reducing E_{loss}. For instance, the wide-bandgap donor polymer D18-Cl (higher-lying HOMO) was incorporated into the PM6:L8-BO blend (Fig. 7A) by Huang et al.[105] An alloy phase formed with PM6, lowering the donor HOMO level (−5.57 eV vs. −5.53 eV). Consequently, V_{OC} was increased and E_{CT} was elevated (Fig. 7B), reducing the $E_g − E_{CT}$ offset. The ternary system exhibited decreased ΔE_2 (0.07 eV vs. 0.08 eV), ΔE_3 (0.207 eV vs. 0.227 eV), and E_{loss} (0.546 eV vs. 0.570 eV), alongside increased V_{OC} (0.91 V vs. 0.87 V) and PCE (19.22%). Similarly, An et al.[106] introduced the small molecule L8-BO as the third component into the B1:BO-4Cl system (Fig. 7C). L8-BO forms an alloy phase with BO-4Cl, increasing the LUMO energy level of the acceptor phase. According to $−kT/q \ln(EQE_{EL})$, the ΔE_3 of the ternary system

decreases from 0.287 eV to 0.274 eV, and E_{loss} reduces from 0.541 eV to 0.530 eV as shown in Fig. 7D. Concurrently, V_{OC} increases from 0.822 V to 0.841 V, with the device's PCE reaching 17.10%. Song et al.[107] introduced BTP-BIO as the third component into the PM6:Y6 system (Fig. 7E). BTP-BIO forms an alloy phase with Y6, causing the acceptor LUMO energy level to increase from −4.10 eV to −4.01 eV. For the ternary device, ΔE_3 decreases from 0.269 eV to 0.239 eV, E_{loss} reduces from 0.584 eV to 0.557 eV, V_{OC} increases from 0.842 V to 0.848 V, and the device's PCE reaches 17.10%.

The cascade energy-level structure can also be constructed by the appropriate incorporation of a third component with tailored energy levels,[108,109] which is able to enhance charge-transfer efficiency through optimizing the driving force while suppressing bimolecular recombination to collectively reduce energy loss. For example, Sun et al.[110] introduced ZY-4Cl as the third component into the PM6:BTP-eC9 system (Fig. 7F), forming a cascaded energy level structure where charge transfer occurs between the donor and the two acceptors, suppressing bimolecular recombination. Meanwhile, it increases the LUMO energy level of the acceptor, enlarging the energy level offset for enhanced V_{OC}. Compared with the PM6:BTP-eC9 device, the PM6:ZY-4Cl:BTP-eC9-based device exhibits decreased ΔE_2 from 0.084 eV to 0.079 eV, reduced ΔE_3 from 0.214 eV to 0.198 eV, and decreased E_{loss} from 0.532 eV to 0.520 eV, with the V_{OC} increasing from 0.844 V to 0.863 V and PCE improving from 17.72% to 18.69%. Similarly, Peng et al.[111] introduced IDIC as the third component into the PM6:TOBDT system, where the ternary blend forms a cascade energy level structure, promoting charge transfer while lowering the HOMO energy level of the donor and increasing the V_{OC}. Compared with the PM6:TOBDT device, the PM6:IDIC:TOBDT-based device shows a decrease in ΔE_3 from 0.249 eV to 0.235 eV, with the V_{OC} increasing from 0.88 V to 0.91 V and PCE improving from 11.0% to 13.7%.

4. Morphology regulation

It is well-known that the active layers of OSCs present complex morphology, including domain size, domain purity, crystallinity, and molecular orientation.[112,113] An optimal morphology features appropriate phase separation to ensure excitons can diffuse to interfaces for dissociation, thereby preventing exciton recombination and associated loss during transport. High crystallinity within the active layer facilitates efficient charge transport pathways, suppressing bimolecular recombination of carriers. Preferential molecular orientation promotes effective separation of CT states into free carriers, which are subsequently collected at the electrodes. Collectively, such a well-tailored morphology suppresses both bimolecular recombination and exciton recombination, leading to reduced energy loss and improving key photovoltaic performance.

4.1 Phase separation structure

Exciton dissociation in OSCs requires diffusion to D/A interfaces within the exciton lifetime, where the built-in electric field subsequently drives charge separation. Excessively large
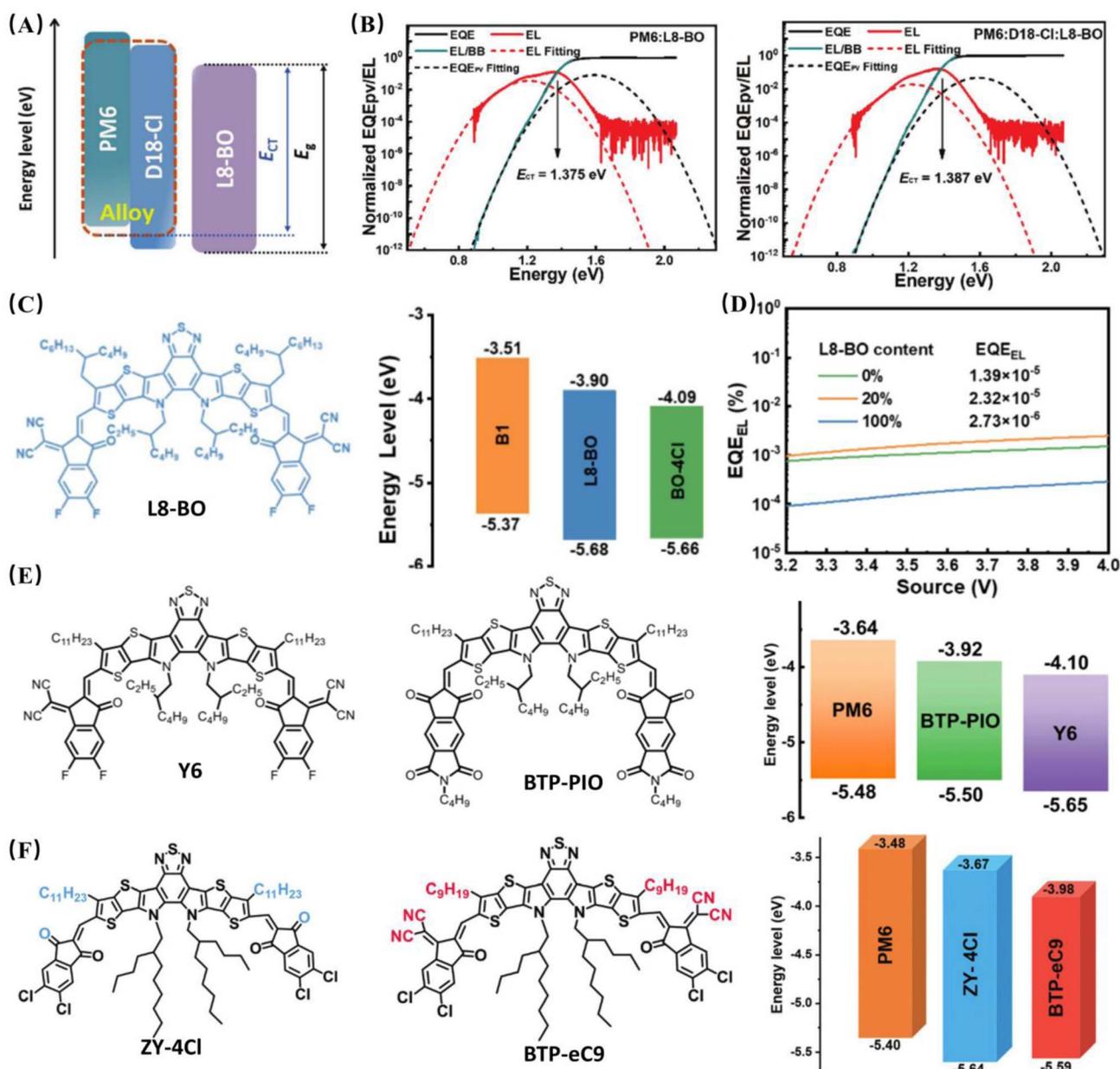
Fig. 7 (A) Energy level of the PM6:D18-Cl:L8-BO ternary system; (B) sEQE and EL spectra of PM6:L8-BO and PM6:D18-Cl:L8-BO devices.[105] Copyright 2022 WILEY-VCH. (C) Chemical structure and energy level diagram of L8-BO; (D) EQE_{EL} values of binary and ternary devices based on B1:BO-4Cl:L8-BO.[106] Copyright 2023 American Chemical Society. (E) Chemical structure and energy level of Y6 and BTP-PIO.[107] Copyright 2024 American Chemical Society. (F) Chemical structure and energy level of ZY-4Cl and BTP-eC9.[110] Copyright 2022 Royal Society of Chemistry.

domain size often causes excitons to recombine before reaching the interface.[114,115] This recombination represents a major energy loss pathway, causing substantial device efficiency loss. Thus, precise domain size control is critical for suppressing bimolecular recombination, minimizing energy loss, and improving device performance.[116,117]

In binary organic systems, intermolecular interactions are modulated through solid additives, enabling active layers with optimized domain size.[54,118] This controlled morphology enhances charge transport while suppressing bimolecular recombination, reducing E_{loss}. For example, DIMCH was added

to PM6:L8-BO binary system by Yang et al.[119] DIMCH exhibits concentrated electrostatic potential (Fig. 8A), demonstrating strong attraction with PM6 and repulsion with L8-BO. Consequently, PM6 crystallinity was enhanced while L8-BO aggregation was suppressed (Fig. 8B), balancing donor–acceptor crystallinity and reducing phase separation. According to Fig. 8C, grazing incidence small-angle X-ray scattering (GISAXS) analysis revealed smaller domain sizes (17.2 nm vs. 23.2 nm with DIO). The optimized morphology suppressed non-radiative recombination, reducing ΔE_2 (0.082 eV vs. 0.087 eV) and ΔE_3 (0.209 eV vs. 0.229 eV) (Fig. 8D). Ultimately, V_{OC} increased
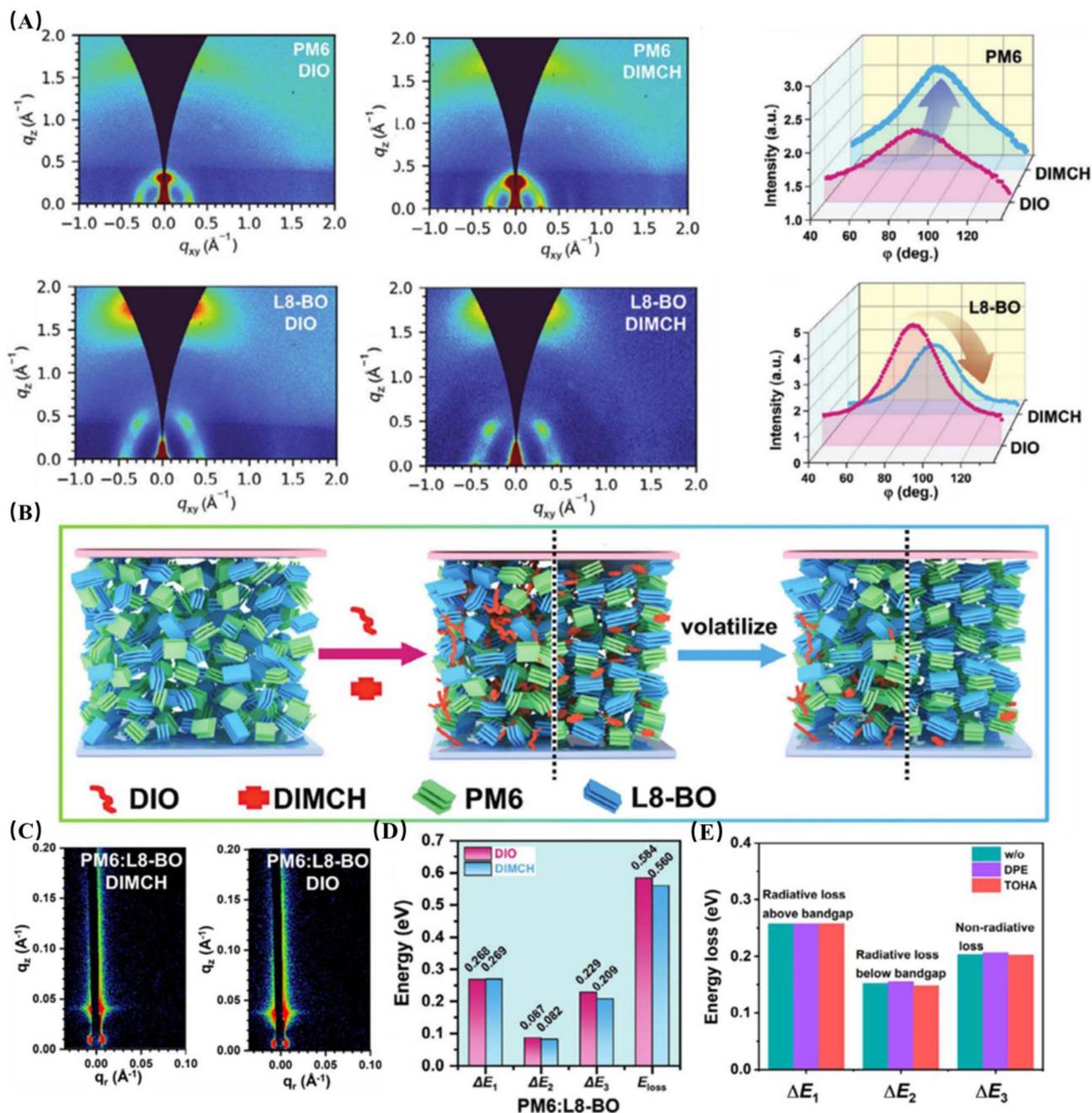
Fig. 8 (A) GIWAXS patterns of PM6 or L8-BO with addition, and pole figure of PM6 and L8-BO; (B) vertical distribution maps of donors and acceptors in BHJ films with addition; (C) GISAXS patterns of BHJ films with DIO or DIMCH addition; (D) energy loss of devices with addition.[119] Copyright 2024 WILEY-VCH. (E) Energy loss of devices treated with different additives.[120] Copyright 2023 WILEY-VCH.

(0.906 V vs. 0.866 V) with an improved PCE of 18.8%. Zhang et al.[120] added 1,8,9-trihydroxyanthracene (TOHA) as a solid additive to the D18-Cl:N3 binary blend system. According to time-of-flight secondary ion mass spectrometry (ToF-SIMS) measurements, phase separation was characterized by comparing changes in the content of characteristic elements. Compared with films without additives, TOHA inhibits the diffusion of D18-Cl and N3, resulting in a uniform phase distribution in the film, thereby improving the phase separation

structure of the active layer and reducing energy loss (Fig. 8E). For a device with TOHA addition, ΔE_3 decreases from 0.152 eV to 0.148 eV, and E_{loss} reduces from 0.613 eV to 0.608 eV. Meanwhile, V_{OC} increases from 0.854 V to 0.862 V, leading to a device PCE of 17.91%.

Introducing polymers as the third component into the system can improve film-forming kinetic behavior and regulate phase separation.[121,122] For example, the polymer acceptor PYIT, which exhibits a narrower bandgap than Y6, was introduced

into the PM6:Y6 binary system by Han *et al.*,[123] forming an optimized ternary system. PYIT crystallizes before Y6, shortening Y6 crystallization time (Fig. 9A). A blue-shifted absorption spectrum was observed in Y6:PYIT blend films relative to Y6 films, indicating suppressed aggregation and reduced acceptor domain size. Absorption spectroscopy (Fig. 9B) revealed a blue shift of the absorption maximum to 810 nm compared to 815 nm in the PM6:Y6 blend, indicating reduced Y6 aggregation. During film formation, a bicontinuous network was formed between PYIT and Y6, promoting exciton dissociation and suppressing bimolecular recombination. Consequently, device E_{loss} was reduced (0.539 eV *vs.* 0.559 eV) and V_{OC} increased (0.864 V *vs.* 0.844 V) (Fig. 9C). Identically, the ternary system achieved 17.05% PCE *versus* 15.40% for PM6:Y6. PC$_{71}$BM was incorporated by Hou *et al.*[124] into the IDIC:DRTB-T binary blend system. Strong acceptor miscibility inhibited IDIC

aggregation, reducing phase separation from 81.4 nm to 15.5 nm. This enhanced exciton dissociation, reduced energy loss, and improved J_{SC}, FF, and PCE. Similarly, domain size within the D18:AQx-2F system was precisely modulated through eC9 introduction, optimizing exciton dissociation and charge transport, as demonstrated by Zhu *et al.*[17] (Fig. 9D), increasing the domain size from 13.4 nm to 20.0 nm, promoting charge transport, suppressing bimolecular recombination, and reducing energy loss (Fig. 9E). Compared with the D18:AQx-2F device, the ΔE_3 of the D18:AQx-2F:eC9-based device decreases from 0.194 eV to 0.180 eV, E_{loss} reduces from 0.533 eV to 0.510 eV, and PCE improves from 19.2% to 20.6%.

Vertical phase separation occurs within the active layer, where the donor concentrates near the anode and the acceptor enriches near the cathode,[11,125] which suppresses bimolecular recombination during carrier transport and reduces overall
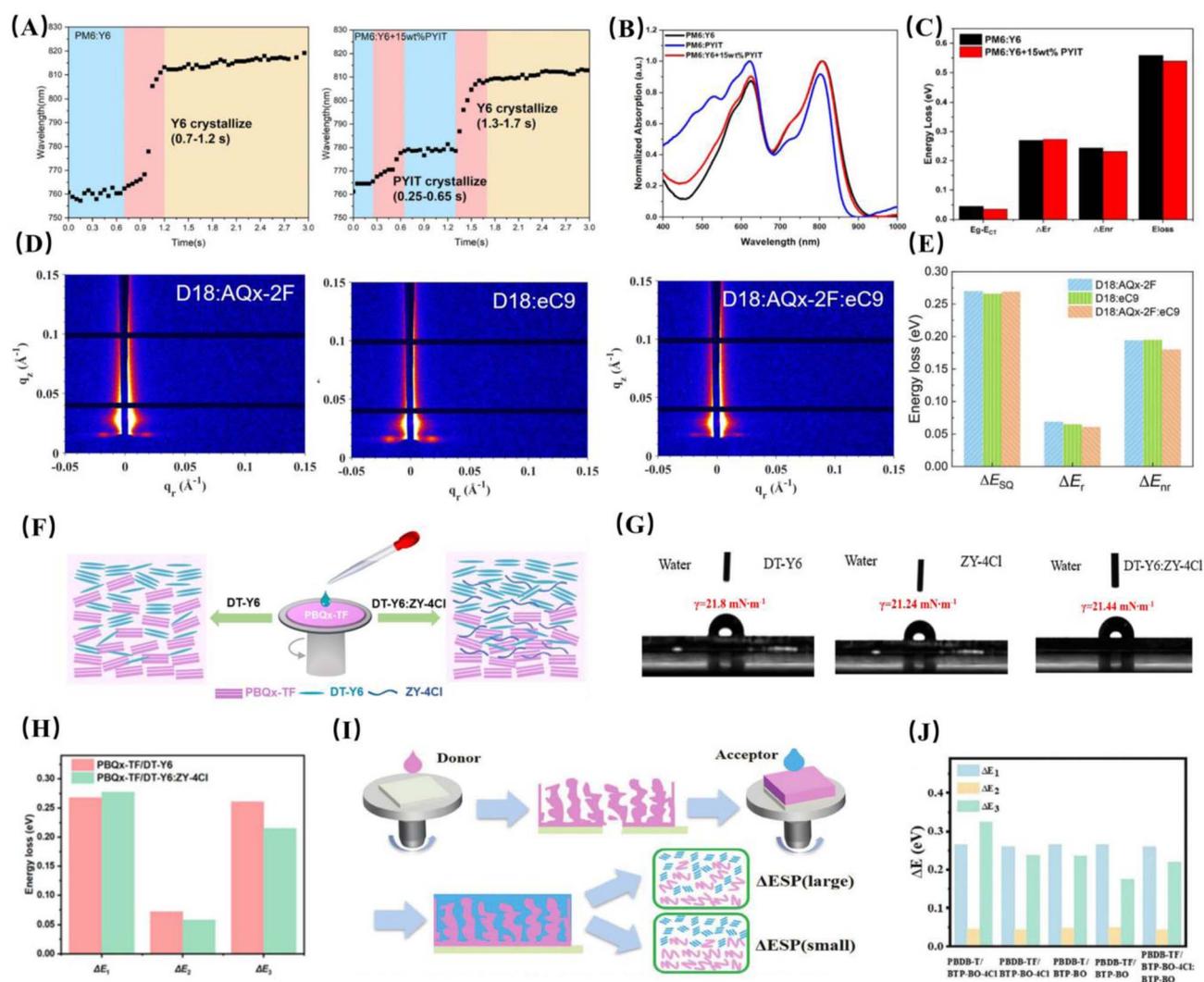

Fig. 9 (A) Absorption peak position of Y6 as a function of time; (B) absorption spectra of binary and ternary films; (C) energy loss of PM6, Y6, and PYIT binary and ternary devices.[123] Copyright 2024 Royal Society of Chemistry. (D) The GISAXS patterns of D18:AQx-2F, D18:eC9, and D18:AQx-2F:eC9 blend films; (E) energy loss of D18, AQx-2F, and eC9 binary and ternary devices.[17] Copyright 2025 WILEY-VCH. (F) Film formation process schematic diagram of the LBL device PBQx-TF/DT-Y6:ZY-4C; (G) contact angle images of DT-Y6, ZY-4Cl, and DT-Y6:ZY-4Cl; (H) energy loss of PBQx-TF device.[126] Copyright 2024 Royal Society of Chemistry. (I) Schematic diagram of active layer formation for PPHJ structures with different electrostatic potentials; (J) energy loss of devices with different systems.[127] Copyright 2024 WILEY-VCH.

device E_{loss}. For example, Huang et al.[126] incorporated ZY-4Cl with a higher LUMO energy level, into the PBQx-TF/DT-Y6 system. Contact angle measurements during spin-coating (Fig. 9F) showed that ZY-4Cl and DT-Y6 exhibit similar γ values (21.24 mN m^{-1} and 21.8 mN m^{-1}, respectively; Fig. 9G), indicating good miscibility between the donor and acceptor materials. However, the γ value of the ZY-4Cl/DT-Y6 mixture (21.44 mN m^{-1}) became significantly higher than that of the donor PBQx-TF (18.8 mN m^{-1}). This increases the surface energy difference and promotes an optimal vertical phase separation structure. Consequently, bimolecular recombination is suppressed, enhancing carrier lifetime and charge mobility. As a result, the devices incorporating PBQx-TF/DT-Y6:ZY-4Cl show increased V_{OC} (0.881 V vs. 0.840 V), reduced E_{loss} (0.55 eV vs. 0.601 eV), and a higher PCE of 19.46% compared to the binary counterpart (Fig. 9H). Similarly, Chen et al.[127] introduced BTP-BO as the third component into the PBDB-TF/BTP-BO-4Cl binary system to optimize the vertical phase separation morphology of the active layer in the binary system. This increases the degree of vertical phase separation in the active layer (Fig. 9I), effectively reducing E_{loss}. Energy loss results in Fig. 9J show that the ΔE_3 of the ternary system decreases from 0.323 eV to 0.219 eV, while the V_{OC} increases from 0.748 V to 0.866 V, with the PCE of the ternary device reaching as high as 19.09%.

4.2 Crystallization

Marcus theory dictates that increased transfer integrals enhance carrier mobility, thereby suppressing bimolecular recombination and mitigating energy loss.[128,129] Research demonstrates that higher crystallinity strengthens intermolecular coupling, leading to increased transfer integrals which consequently enhance charge carrier mobility.[130,131] Crystallization involves sequential nucleation and crystal growth stages, whose precise regulation enables optimal active layer morphology formation.

Additives exhibiting strong intermolecular interactions with donor/acceptor materials regulate material crystal growth,[132,133] achieving optimized morphology and reduced energy loss. For example, TMB was introduced into the PBDB-TF:BTP-eC9 binary system by Hou et al.[114] Opposing electrostatic potentials between TMB and BTP-eC9 promoted strong π–π interactions, which inhibited excessive aggregation while optimizing π–π stacking (Fig. 10A). In the meantime it increased the coherence length (26.96 Å vs. 23.96 Å) and enhanced J_{SC}. TMB volatilization prior to film solidification yielded optimized crystallinity (Fig. 10B). Bimolecular recombination was suppressed by the resulting fibrous network, reducing ΔE_2 (0.296 eV vs. 0.310 eV), ΔE_3 (0.207 eV vs. 0.228 eV), and E_{loss} (0.541 eV vs. 0.563 eV) versus the DIO-treated device. Concurrently, V_{OC} increased (0.854 V vs. 0.837 V) with 18.61% PCE. Li et al.[134] introduced TTBB and TTBI into the PM6/L8-BO binary system, where TTBB enhanced intermolecular interactions with PM6, promoting crystal growth and improving crystallinity. TTBI enabled tighter molecular packing and more ordered arrangement of L8-BO, resulting in a highly crystalline morphological structure in the active layer. Compared with the PM6/L8-BO(DIO) device, the PM6(TTBB)/L8-BO(TTBI) devices showed a decrease in ΔE_3 from 0.24 eV to 0.23 eV, a reduction in E_{loss} from 0.56 eV to 0.54 eV, and an increase in V_{OC} from 0.881 V to 0.898 V, with the device PCE reaching 19.4%. Furthermore, 1,2-dimethylnaphthalene (DMN) was added to Y6 (o-XY) solution by Xie et al.[135] Dual-phase DMN-induced nucleation generated high-crystallinity phase separation in PM6/Y6 (Fig. 10C). This yielded decreased E_{loss} (0.515 eV vs. 0.589 eV), increased V_{OC} (0.849 V vs. 0.764 V), and improved PCE (16.15% vs. 12.76%).

Post-treatment strategies optimize active layer morphology by regulating crystallization behavior.[71,136] During spin-coating, rapid solvent evaporation traps the active layer morphology in a kinetically quenched, thermodynamically metastable state. This metastability is exacerbated by structural similarities between donors and acceptors, which promote poorly crystalline interpenetrating phases. Post-treatment can enhance molecular mobility, enabling redistribution into thermodynamically favorable configurations. Consequently, bimolecular recombination is suppressed and energy loss reduced. For example, solvent vapor annealing (SVA) was applied to the BTTzR:Y6 device by Li et al.[137] GIWAXS analysis revealed increased coherence lengths (CCL(100): 7.14 nm vs. 5.49 nm; CCL(010): 2.61 nm vs. 1.87 nm) and reduced π–π stacking distances (3.50 Å vs. 3.53 Å). The crystalline bicontinuous network reduced ΔE_3 to 0.18 eV and E_{loss} to 0.51 eV, improving PCE from 0.1% to 13.9%. Similarly, sequential TA/SVA treatment was employed on the BSCl:IDIC-4Cl binary blend system by Wei et al.,[138] enhancing OOP crystallinity (CCL(010): 13.8 nm vs. 13.5 nm), yielding reduced ΔE_3 (0.373 eV vs. 0.394 eV) and E_{loss} (0.721 eV vs. 0.745 eV), and in the meantime, increasing V_{OC} (0.865 V vs. 0.845 V) and 13.03% PCE, which is a 23% improvement compared to those of the original device. Ge et al.[121] optimized the active layer morphology of OSCs based on the BT-2F:N3 system through CS$_2$ SVA, improving the crystallinity of the active layer. Compared with the TA-treated device, the ΔE_3 of the CS$_2$ SVA-treated device decreased from 0.244 eV to 0.226 eV, E_{loss} reduced from 0.529 eV to 0.521 eV, V_{OC} increased from 0.829 V to 0.845 V, and the PCE reached 15.39%, which was significantly higher than the 14.66% of the TA-treated device.

Introducing a third component as nuclei to promote heterogeneous nucleation of molecules in the active layer is an effective approach to improve crystallization behavior.[81,139] For example, Bo et al.[139] introduced LA15 as the third component into the D18:L8-BO binary blend system. Its branched alkyl side chains improved molecular planarity and intermolecular interactions, yielding high crystallinity. Acting as nuclei, LA15 induced crystallization of donor polymer D18 while increasing L8-BO coherence length (CCL(010): 20.94 Å vs. 16.58 Å) via GIWAXS. The ternary film formed an interconnected network, establishing efficient electron transport channels that suppressed recombination. Consequently, EQE$_{EL}$ increased (0.063% vs. 0.036%), V_{OC} increased (0.92 V vs. 0.90 V), and ΔE_3 decreased (0.18 eV vs. 0.20 eV), achieving 19.13% PCE. Similarly, the highly crystalline small-molecule donor BTTzR was introduced into the PM6:Y6 binary system by Li et al.,[140] enhancing
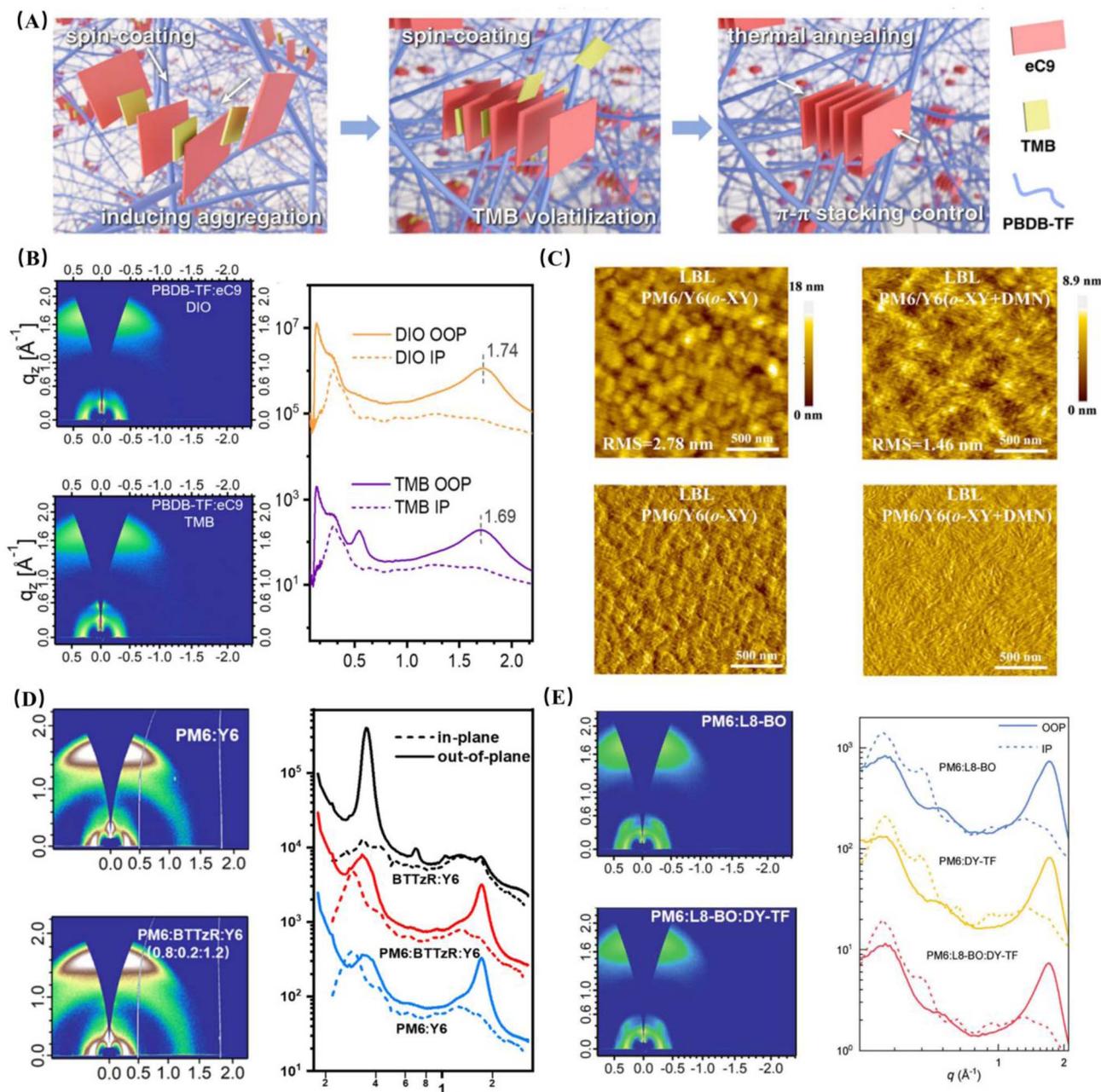
Fig. 10 (A) Schematic diagram of the mechanism of action of the TMB additive during the film formation process; (B) 2D GIWAXS patterns and their scattering curves of PBDB-TF:eC9 films with DIO or TMB addition.[114] Copyright 2023 Royal Society of Chemistry. (C) AFM height images and phase images of PM6/Y6(o-XY) and PM6/Y6(o-XY + DMN) films.[135] Copyright 2019 Royal Society of Chemistry. (D) GIWAXS patterns and the scattering curves of PM6:Y6 and PM6:BTTzR:Y6 films.[140] Copyright 2021 Elsevier. (E) GIWAXS patterns and the scattering curves of PM6:L8-BO and PM6:L8-BO:DY-TF films.[141] Copyright 2023 WILEY-VCH.

active layer crystallinity (Fig. 10D). The ternary device exhibited reduced ΔE_3 (0.19 eV vs. 0.23 eV), lower E_{loss} (0.53 eV vs. 0.57 eV), increased V_{OC} (0.87 V vs. 0.83 V), and 17.7% PCE versus 15.8%. Furthermore, Huang et al.[141] introduced DY-FT into the PM6:L8-BO system; DY-FT has a similar main chain structure and crystal structure to L8-BO, increasing the crystallinity of the acceptor phase (Fig. 10E), which suppresses bimolecular recombination and reduces energy loss. Relative to the binary device, the

ternary device showed a decrease in ΔE_3 from 0.247 eV to 0.228 eV, a reduction in E_{loss} from 0.591 eV to 0.565 eV, an increase in V_{OC} from 0.884 V to 0.905 V, and an improvement in PCE from 18.44% to 19.13%.

4.3 Molecular orientation

Molecular anisotropy in conjugated systems facilitates distinct orientation configurations such as edge-on, face-on, and end-

on. With uniform alignment at D/A interfaces, the built-in electric field can be intensified to promote exciton dissociation, and thereby reduce energy loss.[142,143]

Additive molecules thermodynamically optimize active layer morphology through distinct donor–acceptor interactions,[31,144] inducing molecular reorientation to reduce energy loss and enhance performance. For instance, DBOF was added to the D18:Y6 binary system by Peng et al.[145] Strong π–π interactions with Y6 promoted acceptor rearrangement during volatilization, optimizing vertical donor–acceptor distribution. This yielded the narrowest out-of-plane (010) peak of Y6 films, indicating enhanced face-on orientation and ordered packing (Fig. 11A). The resulting nanoscale interpenetrating network reduced ΔE_3 (0.230 eV vs. 0.250 eV) and E_{loss} (0.533 eV vs. 0.553 eV), while increasing V_{OC} (0.875 V vs. 0.869 V) and achieving 18.60% PCE. Zhan et al.[146] first utilized $CsPb_3$ perovskite quantum dots (PQDs) as additives. In PTB7-Th:FOIC films treated with PQDs, molecules preferentially adopt a face-on orientation (Fig. 11B), which facilitates charge transport. Finally, for OSCs based on the PTB7-Th:FOIC system treated with PQDs, ΔE_2 decreases from 0.120 eV to 0.010 eV, ΔE_3 reduces from 0.311 eV to 0.295 eV, and E_{loss} decreases from 0.607 eV to 0.580 eV. Meanwhile, V_{OC} increases from 0.711 V to

0.740 V, thus improving the PCE of the PTB7-Th:FOIC-based device from 11.6% to 13.2%. Furthermore, the 3D star-shaped Star-A was introduced into the PM6:Y6 binary blend system by Dae Hwan Lee et al.[147] Star-A disrupted intrinsic molecular orientations (edge-on PM6 and face-on Y6), inducing preferential face-on alignment as shown in Fig. 11C. This enhanced exciton dissociation and reduced energy loss, yielding decreased ΔE_3 (0.224 eV vs. 0.240 eV), lower E_{loss} (0.563 eV vs. 0.581 eV), increased V_{OC} (0.856 V vs. 0.835 V), and improved PCE (17.2% vs. 15.6%).

Thermal annealing enables precise regulation of molecular packing within the active layer,[148–150] which mitigates energy loss and consequently enhances device performance. For example, Zhang et al.[151] adopted a rapid thermal annealing (RTA) strategy (Fig. 12A), to optimize the PM6:L8-BO-X blend film, resulting in favorable face-on orientations. GIWAXS analysis revealed enhanced face-on orientations versus thermal annealing (TA), attributed to slower solvent evaporation enabling molecular reorientation. The minimized in-plane (010) peak indicated superior face-on stacking. Optimized D/A morphology with increased interfacial contact promotes exciton dissociation. Consequently, the RTA-treated device (Fig. 12B) exhibited reduced ΔE_2 (0.070 eV vs. 0.076 eV), ΔE_3
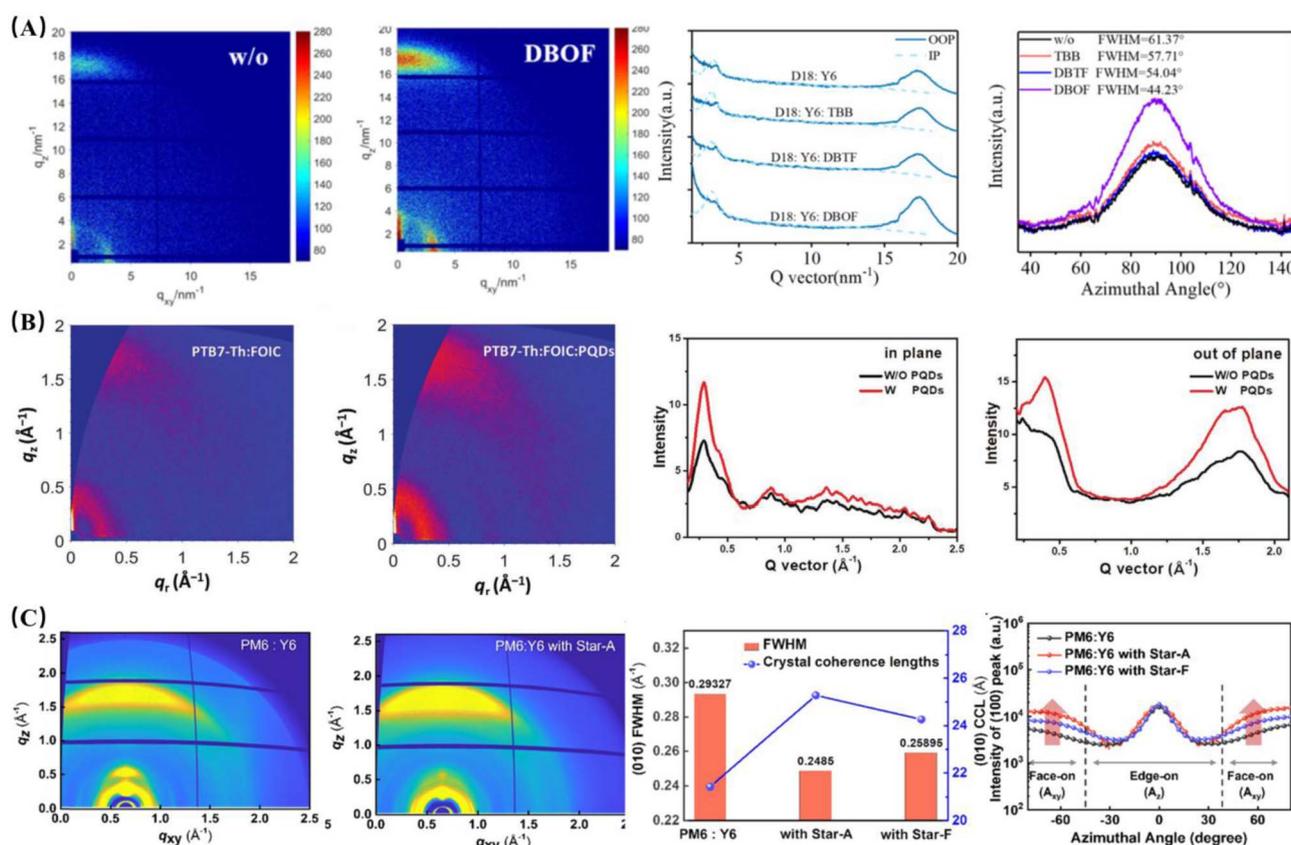
Fig. 11 (A) 2D GIWAXS patterns, their scattering curves, and azimuthal dependence curves around the (010) peak in the 2D GIWAXS patterns of D18:Y6 films without an additive and with DBOF addition.[145] Copyright 2024 Elsevier. (B) 2D GIWAXS patterns and their scattering curves of PTB7-Th:FolC and PTB7-Th:FolC:PQDs films.[146] Copyright 2020 WILEY-VCH. (C) 2D GIWAXS patterns, FWHM, crystalline coherence length plots of the (010) peak, and azimuthal scan plots of the (100) peak in GIWAXS modes of PM6:Y6 films without an additive and with Star-A addition.[147] Copyright 2022 Elsevier.

Fig. 12 (A) Schematic diagrams of the thermal annealing (TA) process and RTA process, and GIWAXS patterns of PM6:L8-BO-X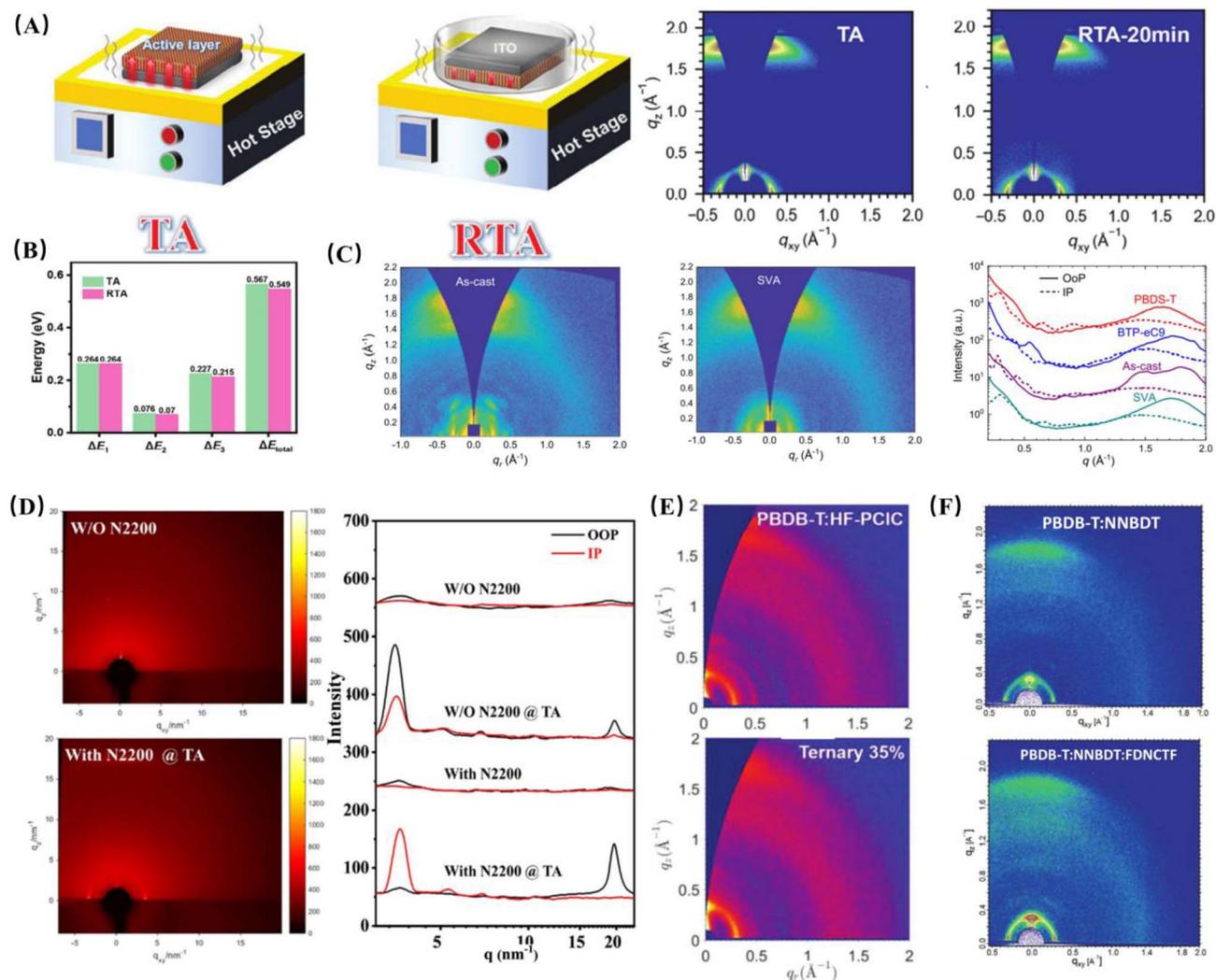 films treated with TA or RTA; (B) energy loss of the PM6:L8-BO-X device treated with TA or RTA.[151] Copyright 2024 WILEY-VCH. (C) 2D GIWAXS patterns and their scattering curves of active layers without annealing or treatment with SVA.[152] Copyright 2022 Elsevier. (D) GIWAXS patterns and their scattering curves of DRCN5T:ITIC-Th and DRCN5T:ITIC-Th:N2200 films.[155] Copyright 2022 WILEY-VCH. (E) 2D GIWAXS patterns of PBDB-T:HF-PCIC and PBDB-T:HF-PCIC:IEICO-4F films.[157] Copyright 2018 WILEY-VCH. (F) 2D GIWAXS patterns of PBDB-T:NNBDT and PBDB-T:NNBDT:FDNCTF films.[158] Copyright 2018 WILEY-VCH.

(0.215 eV vs. 0.227 eV), and E_{loss} (0.549 eV vs. 0.567 eV), alongside increased V_{OC} (0.896 V vs. 0.877 V) and 19.91% PCE versus 18.89%. Zhong et al.[152] employed a fluorinated solvent vapor annealing (FSVA) strategy to optimize the PF7:L8BO blend film, leading most of the molecules in the active layer to adopt a face-on orientation. Compared with the TA-treated device, the FSVA-treated device shows a decrease in ΔE_3 from 0.228 eV to 0.225 eV, a reduction in E_{loss} from 0.554 eV to 0.550 eV, and an improvement in device PCE from 18.68% to 19.09%. Furthermore, SVA was implemented on the PBDS-T:BTP-eC9 binary system by René A. J. Janssen et al.[153] GIWAXS showed decreased in-plane (010) and increased out-of-plane (010) peaks, confirming the dominant face-on orientation versus unannealed films (Fig. 12C). The SVA-treated device achieved 16.4% PCE (vs.

14.7%) with reduced energy loss, with a ΔE_1 of 0.270 eV, ΔE_3 of 0.035 eV, ΔE_3 of 0.226 eV, and E_{loss} of 0.531 eV.

Introducing a third component induces the transformation of donors or acceptors from the edge-on to the face-on orientation.[154,155] For example, the highly crystalline N2200 with a face-on orientation was incorporated into the DRCN5T:ITIC-Th binary system by Liu et al.[156] High lattice matching (93%) with DRCN5T and limited miscibility enabled N2200 to act as nucleation sites. Elevated temperature enhanced DRCN5T diffusion sufficiently to overcome heterogeneous nucleation barriers, inducing the face-on DRCN5T orientation (Fig. 12D). The uniform face-on ternary active layer reduced E_{loss} (0.74 eV vs. 0.79 eV), increased V_{OC} (0.99 V vs. 0.94 V), and achieved 54% relative PCE enhancement. Chen et al.[157] introduced IEICO-4F into the PBDB-T:HF-PCIC system. The absorption peak in the

in-plane (010) direction decreases, while that in the out-of-plane (010) direction increases, indicating that the molecular orientation in the ternary blend film is mainly face-on (Fig. 12E), which promotes exciton dissociation and reduces energy loss. Compared with the binary device, the ternary device exhibits a decrease in ΔE_2 from 0.13 eV to 0.04 eV, a reduction in ΔE_3 from 0.38 eV to 0.28 eV, a decrease in E_{loss} from 0.80 eV to 0.59 eV, and an improvement in device PCE from 8.82% to 11.20%. Chen et al.[158] introduced FDNCTF into the PBDB-T:NNBDT binary system. In the binary blend film, NNBDT is mainly oriented in a face-on manner. FDNCTF has a similar chemical structure and molecular orientation to NNBDT, leading to more molecules in the ternary film transforming into a face-on orientation[159] (Fig. 12F), further reducing energy loss. Compared with the binary device, the ternary device shows a decrease in E_{loss} from 0.55 eV to 0.54 eV, an increase in V_{OC} from 0.880 V to 0.887 V, and an improvement in device PCE from 11.7% to 12.8%.

5. Applied research

The commercialization of OSCs critically depends on advancing scalable fabrication and long-term operational stability-two interconnected pillars of applied research. While laboratory-scale devices continue to achieve remarkable power conversion efficiencies, their performance often deteriorates significantly when scaled to module-level areas due to issues such as increased series resistance, inhomogeneous film formation, and interfacial contact defects.[160] Concurrently, under real-world operating conditions involving thermal stress and illumination, active layer morphologies-especially in state-of-the-art non-fullerene acceptor systems-tend to evolve undesirably, leading to molecular reorientation, phase separation, and increased non-radiative recombination loss.[161] Overcoming these scaling and stability challenges is essential for achieving viable product lifetimes and economic feasibility, thereby accelerating the integration of OPVs into building-integrated photovoltaics and portable energy systems.[162]

5.1 Large area

The reduction in V_{OC} commonly observed during the scaling of organic photovoltaics from lab-scale cells to large-area modules can be partly ascribed to increased energy loss, largely driven by morphological non-uniformity in the photoactive layer.[163,164] The difficulty in maintaining homogeneous molecular packing and film morphology over extended areas results in diminished molecular ordering and a higher density of defects. These structural imperfections serve as recombination sites, enhancing non-radiative recombination loss and thus contributing to greater overall energy loss, which in turn leads to the decline in V_{OC} in scaled devices. For example, Xie et al.[165] introduced the solid additive MN into the PM6/BTP-eC9 system, which induced a molecular reorientation of PM6 from edge-on to face-on stacking, leading to more uniform crystal alignment and facilitating faster exciton dissociation at the donor–acceptor interface. Furthermore, MN enhanced the crystallinity

and promoted tighter molecular packing of PM6, reducing the defect-state density and resulting in an optimized active-layer morphology. Compared to the reference PM6/BTP-eC9 device, the MN-incorporated PM6(MN)/BTP-eC9-based cell exhibited a reduction in energy loss from 0.532 eV to 0.516 eV, an increase in V_{OC} from 0.830 V to 0.850 V, and an improvement in PCE from 16.93% to 18.42%. Additionally, a large-area module (28.82 cm²) based on the PM6(MN)/BTP-eC9 system achieved a PCE of 16.04%, with a V_{OC} of 13.15 V, a J_{SC} of 1.659 mA cm⁻², and an FF of 73.50%.

In large-area devices, the typically thicker active layers result in longer charge transport paths.[166,167] This increased distance inherently increases the probability of charge carrier recombination, leading to greater energy loss. For example, Ge et al.[168] developed a chlorinated analogue, eC9-2Cl, based on the BTP-eC9 acceptor, where the incorporation of chlorine atoms enhances the molecular dipole moment, promoting tighter and more ordered intermolecular packing. To further facilitate large-area module fabrication, the active-layer thickness was reduced, shortening charge transport pathways and suppressing bimolecular recombination, thereby lowering energy loss. Compared to the PCE10:BTP-eC9 large-area module (0.09 cm²), the PCE10:eC9-2Cl-based module exhibits reduced energy loss, with ΔE_2 decreasing from 0.103 eV to 0.080 eV, ΔE_3 from 0.311 eV to 0.264 eV, and total E_{loss} from 0.677 eV to 0.628 eV. The optimized module delivers a V_{OC} of 5.318 V, a J_{SC} of 2.60 mA cm⁻², an FF of 68.15%, and a PCE of 9.42%.

Imperfect interfacial contact in large-area modules impedes charge extraction, leading to localized recombination and increased non-radiative energy loss.[169] For example, Zheng et al.[170] developed a self-assembled monolayer (SAM), termed 4BCP, which features an asymmetric even-carbon alkyl chain that imparts high solubility and an enhanced dipole moment. This molecular design enables uniform and dense coverage on indium tin oxide (ITO) electrodes, effectively minimizing contact defects at the interface with the active layer. The optimized contact facilitates efficient charge collection by the electrode, suppresses localized recombination, and reduces energy loss. As a result, the PM6:BTP-eC9-based device incorporating 4BCP achieved a PCE of 19.7%. Moreover, a large-area device (1.10 cm²) with the same configuration attained a PCE of 17.2%, with a V_{OC} of 0.876 V, a J_{SC} of 26.4 mA cm⁻², and an FF of 74.4%.

5.2 Stability

In OSCs, efficiency degradation is fundamentally linked to morphological instability, primarily manifested through increased domain size and unfavorable molecular reorientation. These morphological changes reduce the donor–acceptor interfacial area, impede charge transport, and enhance non-radiative recombination, collectively contributing to significant energy loss.[171] The reorientation of polymer donors from the edge-on to face-on configuration exemplifies this degradation mechanism, operating through two parallel pathways: an upshift of the polymer HOMO level that reduces the built-in potential and increases non-radiative recombination,

leading to V_{OC} loss, and exacerbated phase separation that disrupts acceptor phase continuity, causing a substantial decrease in electron mobility and consequent FF degradation. Consequently, stabilizing the active layer morphology represents an essential strategy for maintaining device performance and operational stability.[172]

Enhancing device stability can be achieved by suppressing the growth of phase-separated domains, as excessive domain size impedes charge transport and promotes recombination, which are primary drivers of performance degradation.[173] For instance, Li et al.[27] developed an asymmetric acceptor, BTP-eC9-4ClO, based on the BTP-eC9 structure. GISAXS measurements revealed a reduction in the $2R_g$ from 31.2 nm for the PM6:BTP-eC9 blend to 21.1 nm for the PM6:BTP-eC9-4ClO blend, indicating finer phase separation in the latter. This suppressed phase aggregation facilitates efficient charge transport, reduces bimolecular recombination, and lowers energy loss, while simultaneously enhancing device stability. Compared to the PM6:BTP-eC9-based device, the PM6:BTP-eC9-4ClO-based device exhibited a decrease in ΔE_3 from 0.202 eV to 0.179 eV and a reduction in total E_{loss} from 0.555 eV to 0.530 eV, accompanied by an improvement in V_{OC} from 0.861 V to 0.891 V and an increase in PCE from 19.12% to 20.03%. The optimized device also demonstrated exceptional thermal stability, with a T_{80} lifetime of 7834 hours under heating at 80 °C in a nitrogen atmosphere-significantly exceeding the 395 hours observed for the control device.

Suppressing the detrimental molecular reorientation enhances operational stability by preserving efficient charge transport pathways and minimizing degradation from recombination.[174] For example, Chen et al.[175] introduced a gradient thermal annealing strategy to regulate the molecular orientation and crystallinity of the polymer donor PM6. This process promoted a transition toward face-on molecular stacking in the bulk-heterojunction blend, facilitating charge transport and reducing energy loss while enhancing device stability. In the PM6:BO-4Cl system, the optimized crystallization behavior of PM6 suppressed its excessive diffusion into the acceptor phase, thereby preserving a well-interpenetrated donor–acceptor network. Compared to the control device, the gradient-annealed device exhibited a reduction in ΔE_2 from 0.061 eV to 0.056 eV, a decrease in ΔE_3 from 0.219 eV to 0.212 eV, and a lowering of total E_{loss} from 0.541 eV to 0.528 eV, accompanied by an increase in V_{OC} from 0.847 V to 0.857 V and an improvement in PCE from 17.25% to 18.22%. Furthermore, the treated device demonstrated superior operational stability, retaining 91.6% of its initial PCE after 300 hours of continuous illumination under a nitrogen atmosphere, outperforming the control device which maintained 86.1%.

6. Conclusion and outlook

This review systematically summarizes recent advances in minimizing energy loss in OSCs, introducing the fundamental mechanisms governing energy loss pathways, and discussing the operating principles and implementation approaches of two critical modulation strategies. Subsequently, it focuses on two

critical optimization pathways: energy level regulation by ingenious design of material energy levels through molecular synthesis, or reshaping the active layer energy level structure via ternary strategies, and morphology regulation by precise tuning of the phase separation scale and structure, enhancement of material crystalline order, and guidance of molecular orientation. We further reveal how these strategies significantly shape the photovoltaic performance of the device, particularly their key efficacy in reducing energy loss. We analyze how energy loss responds to subtle changes in material energy levels and its relationship with key morphological parameters, aiming to substantially reduce energy loss and enable OSCs to achieve high energy conversion efficiency. Despite significant progress in reducing energy loss in OSCs, there are still multiple challenges in translating laboratory research into practical applications. Future research must converge on elucidating molecular mechanisms underlying multidimensional regulatory processes, designing integrated materials that simultaneously achieve high efficiency and operational stability, and developing precision strategies to suppress non-radiative recombination. The synergistic priorities establish an essential pathway toward OSCs with ultralow energy loss.

Current optimization strategies predominantly address energy level modulation and morphological control as separate domains, whereas the reciprocal interaction mechanisms between these two regulatory dimensions remain inadequately elucidated. For example, subtle modifications of molecular energy levels may affect crystallization processes through altered intermolecular interactions, while morphological evolution may in turn influence frontier orbital energetics, as exemplified by π–π stacking modulation of HOMO and LUMO energy levels. Future research must establish a dynamic "energy level-morphology-performance" correlation model integrated with in situ characterization techniques to elucidate real-time coupled evolution of electronic and structural properties during material synthesis and film formation, enabling precise synergistic control of multiple parameters.

Despite being achieved primarily through elaborate molecular modifications or complex post-treatments, the long-term stability and compatibility with large-scale manufacturing processes of existing high-performance systems remain significant limitations. On one hand, it is necessary to develop donor–acceptor materials with intrinsic high stability; for instance, strategies such as rigid backbone design and side-chain cross-linking can be employed to suppress molecular aggregation-induced degradation. On the other hand, exploration of "self-assembling" active layer systems should be conducted, utilizing specific intermolecular interactions (e.g., hydrogen bonds and halogen bonds) to achieve ideal morphologies without complex post-treatments, thus balancing efficiency and fabrication cost. Meanwhile, stabilization of ternary and multicomponent systems requires rigorous characterization of long-term phase separation dynamics among constituents, along with the development of thermodynamically stable alloy-like phases.

Furthermore, a significant gap persists between the practical energy loss in OSCs and the theoretical limit, with ΔE_3 accounting for over 30% of total loss representing a major

obstacle toward reaching the S–Q limit. Current understanding remains largely macroscopic. Future efforts should integrate quantum chemical calculations with single-molecule spectroscopy to establish a comprehensive model linking "molecular packing–defects–non-radiative decay", and employ techniques such as transient absorption spectroscopy to elucidate energy dissipation pathways. Concurrently, tackling challenges including defect modulation and energy level alignment will be essential to reduce non-radiative loss below 100 meV, thereby enabling the synergy of high V_{OC} and high J_{SC}.

To achieve higher PCE, future research should focus on synergistically minimizing energy loss while enhancing photon harvesting and charge collection capabilities. Key priorities include developing novel narrow-bandgap materials to broaden spectral response, employing multilayer architectures or photon management techniques to improve light absorption, and incorporating dipole-interfacial layers to optimize energy-level alignment and suppress non-radiative recombination. Advanced *in situ* characterization methods are needed to resolve film formation dynamics and morphological evolution, enabling precise control over active layer aggregation. Furthermore, integrating large-area fabrication processes with stability studies is essential to maintain high performance under real-world operating conditions. A systematic approach combining material design, structural optimization, and process innovation will be crucial to push the PCE of organic solar cells toward the theoretical limit of 25% and beyond, laying a solid foundation for their commercial application.

Author contributions

Conceptualization: Jiangang Liu and Jingming Xin; formal analysis: Zefeng Liu; funding acquisition: Jiangang Liu; investigation: Zefeng Liu, Xingpeng Liu, Yutong Zhang, Mingzhi Duan, Yan Zhang, Zhenhui Xu and Junzheng Yan; methodology: Qiuju Liang; project administration: Zemin He; supervision: Jiangang Liu and Jingming Xin; validation: Zefeng Liu and Jingming Xin; writing-original draft: Zefeng Liu and Jiangang Liu; writing-review & editing: Zefeng Liu and Jingming Xin.

Conflicts of interest

The authors declare no conflicts of interest.

Data availability

The data supporting this article have been included within the article. No new data were generated or analyzed as part of this review.

Acknowledgements

Notes and references

1 Z. Bi, B. Wu, K. Wang, J. Xue, C. Liu, L. Tang, K. Zhou, L. Jiang and W. Ma, *Adv. Sci.*, 2025, **12**, 2502077.

2 C. Chen, L. Wang, W. Xia, K. Qiu, C. Guo, Z. Gan, J. Zhou, Y. Sun, D. Liu, W. Li and T. Wang, *Nat. Commun.*, 2024, **15**, 6865.

3 J. Chen, Y. Wu, L. Chen, Y. Liao, Y. Zhu, A. Saparbaev, M. Wan, J. Wu, Y. Li, H. Xiang, A. Saidkulova, X. Wang and R. Yang, *Adv. Funct. Mater.*, 2025, e08397, DOI: **10.1002/adfm.202508397**.

4 Z. Dai, C. Duan, Q. Guo, Z. Wang, N. Jiang, Y. Ding, L. Gao and E. Zhou, *Battery Energy*, 2024, **3**, 20230065.

5 B. Deng, Y. Li, Z. Lu, K. Zheng, T. Xu, S. Wang, X. Luo, B. Grandidier, J. Zhang and F. Zhu, *Nat. Commun.*, 2025, **16**, 597.

6 X. Dong, B. Lee, R. Song, J. Neu, S. Kashani, W. You and H. Ade, *Adv. Energy Mater.*, 2024, 2404962, DOI: **10.1002/aenm.202404962**.

7 X. Duan, J. Song, J. Zhang, J. Zhuang, J. Deng, X. Wang, G. Dai, B. Song, J. Qiao, X. Hao, J. Zhang, R. Yang, G. Lu, F. Liu and Y. Sun, *Adv. Mater.*, 2025, 2503510.

8 J. Fu, Q. Yang, P. Huang, S. Chung, K. Cho, Z. Kan, H. Liu, X. Lu, Y. Lang, H. Lai, F. He, P. W. K. Fong, S. Lu, Y. Yang, Z. Xiao and G. Li, *Nat. Commun.*, 2024, **15**, 1830.

9 Y. Ge, Y. Wu, Y. Hai, X. Li, T. Pan, T. A. Dela Pena, J. Wu, Y. Li, H. Yang, C. Cui and Y. Li, *Adv. Mater.*, 2025, **37**, 2502579.

10 J. Hao, Y. Feng, Q. Ma, H. Li, C. Hong, C. Hou, Y. Wang, Y. Jing, Y. Li, G. Liu, X. Li, A. Li, F. Bian, R. Ma, Y. Wang, Y. Huang and C. Yang, *Adv. Sci.*, 2025, e01823, DOI: **10.1002/advs.202501823**.

11 D. He, F. Zhao, C. Wang and Y. Lin, *Adv. Funct. Mater.*, 2022, **32**, 2111855.

12 Z. Huang, Y. Xu, L. Liu, J. Xie, H. Li, Z. Yang, K. Zhang and F. Huang, *J. Mater. Chem. A*, 2025, **13**, 15574–15584.

13 C. M. Hung, J. H. Shi, H. C. Tsai, C. P. Lin, B. H. Chen, S. D. Yang and P. T. Chou, *J. Am. Chem. Soc.*, 2025, **147**, 23683–23695.

14 J. N. Ike, G. T. Mola and R. T. Taziwa, *Chem. Afr.*, 2025, **8**, 2687–2705.

15 Y. Ji, L. Liang, T. Chen, X. Liu, M. Mao, Y. Hu, Y. Jin, X. Huang, X. Ren, D. Xie, R. Hu, Y. Zhang, X. Yang and W. Huang, *Adv. Energy Mater.*, 2025, 2501698, DOI: **10.1002/aenm.202501698**.

16 Q. Jiang, X. Yuan, Y. Li, Y. Luo, J. Zhu, F. Zhao, Y. Zhang, W. Wei, H. Feng, H. Li, J. Wu, Z. Ma, Z. Tang, F. Huang, Y. Cao and C. Duan, *Angew. Chem.*, 2025, **64**, e202416883.

17 Y. Jiang, K. Liu, F. Liu, G. Ran, M. Wang, T. Zhang, R. Xu, H. Liu, W. Zhang, Z. Wei, Y. Cui, X. Lu, J. Hou and X. Zhu, *Adv. Mater.*, 2025, **37**, 2500282.

18 C. Li, J. Song, H. Lai, H. Zhang, R. Zhou, J. Xu, H. Huang, L. Liu, J. Gao, Y. Li, M. H. Jee, Z. Zheng, S. Liu, J. Yan, X. K. Chen, Z. Tang, C. Zhang, H. Y. Woo, F. He, F. Gao, H. Yan and Y. Sun, *Nat. Mater.*, 2025, **24**, 433–443.

19 C. Li, J. Zhou, J. Song, J. Xu, H. Zhang, X. Zhang, J. Guo, L. Zhu, D. Wei, G. Han, J. Min, Y. Zhang, Z. Xie, Y. Yi, H. Yan, F. Gao, F. Liu and Y. Sun, *Nat. Energy*, 2021, **6**, 605–613.

20 H. Li, L. Liu, J. Yu, J. Xie, Y. Bai, Z. Yang, M. Dong, K. Zhang, F. Huang and Y. Cao, *Adv. Funct. Mater.*, 2025, 2505226, DOI: **10.1002/adfm.202505226**.

21 J. Li, L. Wang, C. Zhang, H. Wang, Y. Pan, S. Li, X. K. Chen, T. Jia and K. Wang, *Angew. Chem.*, 2024, **63**, e202402726.

22 T. Li, G. Yao, J. Wang, W. Zhong, Z. He and Y. Cao, *ACS Appl. Mater. Interfaces*, 2025, **17**, 33935–33943.

23 M. Liu, L. Wu, Y. Hai, Y. Luo, Y. Li, R. Chen, Y. Ma, T. Jia, Q. Li, S. Liu, R. Ma, Y. P. Cai, J. Wu, G. Li and S. Liu, *Adv. Mater.*, 2025, 2503702, DOI: **10.1002/adma.202503702**.

24 C. Luo, D. Xia, J. Wu, J. Fang, Q. Xie, Y. Zhang, X. Jiang, L. Wan, S. You, L. Jiang, W. Li and C. Zhao, *Energy Fuels*, 2025, **39**, 4030–4037.

25 H. Niu, C. Xiao, J. Xu, H. Fan, Z. Lu, S. Liang, C. R. McNeill, H. Cheng and W. Li, *Adv. Funct. Mater.*, 2025, 2507635, DOI: **10.1002/adfm.202507635**.

26 X. Ran, C. Zhang, D. Qiu, A. Tang, J. Li, T. Wang, J. Zhang, Z. Wei and K. Lu, *Adv. Mater.*, 2025, 2504805, DOI: **10.1002/adma.202504805**.

27 R. Ma, B. Zou, Y. Hai, Y. Luo, Z. Luo, J. Wu, H. Yan and G. Li, *Adv. Mater.*, 2025, **37**, 2500861.

28 S. Shen, W. Liu, H. Lu, W. Zhang, F. Zhao, B. Hu, Z. Suo, K. Zhao, J. Deng, Y. Mi, S. Yuan, Z. Ma, Y. Chen, Y. Liu, Z. Ma, G. Lu, X. Wan, Z. Bo and J. Song, *Adv. Funct. Mater.*, 2025, 2507288, DOI: **10.1002/adfm.202507288**.

29 F. Sun, J. Wu, B. Cheng, L. Kan, F. Hua, W. Sun, H. Wang, Y. Huo, S. Chen, X. Xia, X. Du, F. Liu, E. Wang, X. Guo, Y. Li and M. Zhang, *Energy Environ. Sci.*, 2025, **18**, 7071–7081.

30 B. Cheng, X. Xia, S. Cheng, C. Han, F. Sun, Z. Fu, W. Hou, F. Hua, H. Wang, W. Sun, Y. Huo, S. Ji, X. Guo, H. Yin, X. Du, X. Hao, Y. Li and M. Zhang, *Adv. Mater.*, 2025, **37**, 2500357.

31 Y. Sun, L. Wang, C. Guo, J. Xiao, C. Liu, C. Chen, W. Xia, Z. Gan, J. Cheng, J. Zhou, Z. Chen, J. Zhou, D. Liu, T. Wang and W. Li, *J. Am. Chem. Soc.*, 2024, **146**, 12011–12019.

32 H. Wang, B. Zhang, L. Wang, X. Guo, L. Mei, B. Cheng, W. Sun, L. Kan, X. Xia, X. Hao, T. Geue, F. Liu, M. Zhang and X. K. Chen, *Angew. Chem.*, 2025, **64**, e202508257.

33 Y. Wang, C. Gao, W. Lei, T. Yang, Z. Liang, K. Sun, C. Zhao, L. Chen, L. Zhu, H. Zeng, X. Sun, B. He, H. Hu, Z. Tang, M. Qiu, S. Li, P. Han and G. Zhang, *Nano-Micro Lett.*, 2025, **17**, 206.

34 Y. Wang, J. Wen, Z. Shang, Y. Zhong, H. Zhang, W. Liu, W. Han, H. Yang, J. Liu, J. Zhang, H. Li and Y. Liu, *Angew. Chem.*, 2025, **137**, e202506252.

35 Z. Wei, Y. Wang, Y. Li, S. Gong, X. Jiang, Y. Liu, D. Zhang, Y. Cho, A. Zhang, L. Gao, Y. Cheng, H. Lu, H. Li, Y. Liu, Y. Yao, C. Zhang, Q. Liu, P. Cheng, A. Facchetti, Z. Bo and T. J. Marks, *Joule*, 2025, **9**, 101996.

36 H. Yang, W. Zhang, X. Li, Y. Yuan, Y. Wu, X. Xiong, C. Cui and Y. Li, *Angew. Chem.*, 2025, e202507294, DOI: **10.1002/anie.202507294**.

37 Y. Yang, Q. Wang, Y. Hou, C. Yang, W. Shen and J. Tang, *Org. Electron.*, 2025, **144**, 107262.

38 R. Zeng, F. Han, W. Zhong, M. Zhang, S. Tan, Y. Lin, J. Deng, G. Zhou, L. Kan, L. Zhu, X. Gao, J. Zhu, W. Zhao, S. Xu, X. Xue, B. Hao, Z. Zhou, X. Wu, C. Wang, Z. Fink, Z. Tang, H. Jing, T. P. Russell, Y. Zhang and F. Liu, *Adv. Mater.*, 2025, **37**, 2501812.

39 G. Zhang, X. K. Chen, J. Xiao, P. C. Y. Chow, M. Ren, G. Kupgan, X. Jiao, C. C. S. Chan, X. Du, R. Xia, Z. Chen, J. Yuan, Y. Zhang, S. Zhang, Y. Liu, Y. Zou, H. Yan, K. S. Wong, V. Coropceanu, N. Li, C. J. Brabec, J. L. Bredas, H. L. Yip and Y. Cao, *Nat. Commun.*, 2020, **11**, 3943.

40 P. Zhang, N. Gao, B. Du, Z. Xu, S. Wu, K. Zhu, X. Ma, H. Bin and Y. Li, *Angew. Chem.*, 2025, **64**, e202424430.

41 Y. Zhang, S. Cheng, M. Chang, L. Wang, H. Gao, Z. Wang, G. Lu, S. Gan, X. Lv, J. Wang, Q. Sun, M. Niu, Z. Shen, Z. Wu, C. Yang, X. Liu and L. Meng, *Adv. Sci.*, 2025, e06606, DOI: **10.1002/advs.202506606**.

42 Z. Zhao, S. Chung, L. Bai, J. Zhang, Y. Liu, L. Tan, A. Azeez, Y. Huang, E. Ok, K. Cho, Z. Kan and S. Karuthedath, *Adv. Funct. Mater.*, 2025, 2506593, DOI: **10.1002/adfm.202506593**.

43 X. Zhu, C. Gu, Y. Cheng, H. Lu, X. Wang, G. Ran, W. Zhang, Z. Tang, Z. Bo and Y. Liu, *Adv. Mater.*, 2025, 2507529, DOI: **10.1002/adma.202507529**.

44 P. Bi, S. Zhang, Z. Chen, Y. Xu, Y. Cui, T. Zhang, J. Ren, J. Qin, L. Hong, X. Hao and J. Hou, *Joule*, 2021, **5**, 2408–2419.

45 N. T. Bui and J. J. Urban, *Joule*, 2021, **5**, 2251–2253.

46 Z. Chen, W. Song, K. Yu, J. Ge, J. Zhang, L. Xie, R. Peng and Z. Ge, *Joule*, 2021, **5**, 2395–2407.

47 C. Choi, K. Robert, G. Whang, P. Roussel, C. Lethien and B. Dunn, *Joule*, 2021, **5**, 2466–2478.

48 T. Cui, Y. Zhang, X. Fei, Y.-T. Ding, Z.-Q. Zhang, T. Wang, C.-L. Sun, Q. Zhu, J. Xin, S. Seibt, W. Ma and H.-L. Zhang, *ACS Appl. Energy Mater.*, 2022, **5**, 13861–13870.

49 X. Gu, Y. Wei, N. Yu, J. Qiao, Z. Han, Q. Lin, X. Han, J. Gao, C. Li, J. Zhang, X. Hao, Z. Wei, Z. Tang, Y. Cai, X. Zhang and H. Huang, *CCS Chem.*, 2023, **5**, 2576–2588.

50 M. Ahmed, Y. Zheng, A. Amine, H. Fathiannasab and Z. Chen, *Joule*, 2021, **5**, 2296–2322.

51 I. Burgués-Ceballos, L. Lucera, P. Tiwana, K. Ocytko, L. W. Tan, S. Kowalski, J. Snow, A. Pron, H. Bürckstümmer, N. Blouin and G. Morse, *Joule*, 2021, **5**, 2261–2272.

52 Y. N. Chen, M. Li, Y. Wang, J. Wang, M. Zhang, Y. Zhou, J. Yang, Y. Liu, F. Liu, Z. Tang, Q. Bao and Z. Bo, *Angew. Chem.*, 2020, **59**, 22714–22720.

53 Y. Cui, H. Yao, J. Zhang, T. Zhang, Y. Wang, L. Hong, K. Xian, B. Xu, S. Zhang, J. Peng, Z. Wei, F. Gao and J. Hou, *Nat. Commun.*, 2019, **10**, 2515.

54 T. Dai, Y. Meng, Z. Wang, J. Lu, Z. Zheng, M. Du, Q. Guo and E. Zhou, *J. Am. Chem. Soc.*, 2025, **147**, 4631–4642.

55 M. Ismail Saqib, X. Yin, Z. Liu, M. Zhao, M. Cheng, Y. Li, C. Song, Q. Liang, J. Xin, Z. Miao and J. Liu, *Macromol. Chem. Phys.*, 2025, **226**, 2500031.

56 Q. Liang, Z. Miao, X. Liu, Z. Liu, Z. Xu, Y. Zhang, Z. Zhang, W. Zhai, C. Song, J. Xin, X. Yin and J. Liu, *SusMat*, 2025, **5**, e70003.

57 X. Liu, Y. Zhang, S. Fu, L. Wan, H. Wang, Y. Zhang, Z. Liu, J. Peng, J. Li, C. Song, Z. Miao, Q. Liang and J. Liu, *Adv. Funct. Mater.*, 2025, 2500975, DOI: 10.1002/adfm.202500975.

58 J. Xin, Z. He, Z. Liu, X. Liu, H. Zhu, Z. Zhang, C. Song, X. Yin, Q. Liang and J. Liu, *Small*, 2025, **21**, 2409411.

59 J. Zhu, R. Zeng, E. Zhou, C. Li, J. Deng, M. Du, Q. Guo, M. Ji, Z. Wang, Y. Lin, F. Han, J. Zhuang, S. Tan, L. Kan, L. Zhu, M. Zhang and F. Liu, *J. Am. Chem. Soc.*, 2025, **147**, 24491–24501.

60 W. Wang, Q. Wu, R. Sun, J. Guo, Y. Wu, M. Shi, W. Yang, H. Li and J. Min, *Joule*, 2020, **4**, 1070–1086.

61 Q. An, W. Gao, F. Zhang, J. Wang, M. Zhang, K. Wu, X. Ma, Z. Hu, C. Jiao and C. Yang, *J. Mater. Chem. A*, 2018, **6**, 2468–2475.

62 H. Chen, X. Cao, X. Xu, C. Li, X. Wan, Z. Yao and Y. Chen, *Chin. J. Polym. Sci.*, 2022, **40**, 921–927.

63 R. Hou, M. Li, X. Ma, H. Huang, H. Lu, Q. Jia, Y. Liu, X. Xu, H. B. Li and Z. Bo, *ACS Appl. Mater. Interfaces*, 2020, **12**, 46220–46230.

64 J. Iqbal, *J. Phys. Chem. Solids*, 2025, **200**, 112612.

65 Y. Lang, H. Lai, Y. Fu, R. Ma, P. W. K. Fong, H. Li, K. Liu, X. Yang, X. Lu, T. Yang, G. Li and F. He, *Adv. Mater.*, 2025, **37**, 2413270.

66 J. Li, C. Zhang, X. Sun, H. Wang, H. Hu, K. Wang and M. Xiao, *Nano Energy*, 2024, **125**, 109542.

67 J.-N. Li, M. Cui, J. Dong, W. Jing, J. Bao, Z. Liu, Z. Ma and X. Gao, *Dyes Pigm.*, 2021, **188**, 109162.

68 X. Li, R. Peng, Y. Qiu, Y. Zhang, J. Shi, S. Gao, H. Liu, F. Jin and Z. Ge, *Adv. Funct. Mater.*, 2024, **35**, 2413259.

69 T. Zhao, H. Wang, M. Pu, H. Lai, H. Chen, Y. Zhu, N. Zheng and F. He, *Chin. J. Chem.*, 2021, **39**, 1651–1658.

70 Z. Li, X. Wang, N. Zheng, A. Saparbaev, J. Zhang, C. Xiao, S. Lei, X. Zheng, M. Zhang, Y. Li, B. Xiao and R. Yang, *Energy Environ. Sci.*, 2022, **15**, 4338–4348.

71 S. Liu, J. Yuan, W. Deng, M. Luo, Y. Xie, Q. Liang, Y. Zou, Z. He, H. Wu and Y. Cao, *Nat. Photonics*, 2020, **14**, 300–305.

72 Y. Zhang, L. Pan, Z. Peng, W. Deng, B. Zhang, X. Yuan, Z. Chen, L. Ye, H. Wu, X. Gao, Z. Liu, C. Duan, F. Huang and Y. Cao, *J. Mater. Chem. A*, 2021, **9**, 13522–13530.

73 Y. Shi, Y. Chang, K. Lu, Z. Chen, J. Zhang, Y. Yan, D. Qiu, Y. Liu, M. A. Adil, W. Ma, X. Hao, L. Zhu and Z. Wei, *Nat. Commun.*, 2022, **13**, 3256.

74 J. Chen, D. Li, M. Su, Y. Xiao, H. Chen, M. Lin, X. Qiao, L. Dang, X. C. Huang, F. He and Q. Wu, *Angew. Chem.*, 2023, **62**, e202215930.

75 J. Chen, H. Wang, S. Mo, H. Chen, X. He, M. Su, D. Li, Y. Xiao, Z. Wang, F. Ye, M. Li, L. Dang, X.-C. Huang, C.-Z. Li, F. He and Q. Wu, *CCS Chem.*, 2024, **6**, 2318–2332.

76 H. Fu, Q. Fan, W. Gao, J. Oh, Y. Li, F. Lin, F. Qi, C. Yang, T. J. Marks and A. K. Y. Jen, *Sci. China: Chem.*, 2021, **65**, 309–317.

77 X. Zhang, X. Wu, J. Zhang, X. Kong, R. Sun, J. Li, A. Li, Z. Li, J. Min, C. Song, Y. Li and C. Sun, *ACS Appl. Energy Mater.*, 2025, **8**, 4527–4536.

78 J.-H. Park, J. Kim, J. H. Kim, D. W. Kim, C. H. Ryoo, O. K. Kwon, C. Lee, J. E. Kwon and S. Y. Park, *ACS Appl. Energy Mater.*, 2020, **4**, 259–267.

79 H. Peng, J. Liang, Y. Zhou, Z. Zhu, J. Guan, P. Guo, X. Wang, R. Yang, E. Wang and Y. Xia, *J. Mater. Chem. C*, 2025, **13**, 6416–6424.

80 F. Yang, H. Fang, E. Guo, C. Xiao, Z. Lu, Y. Wang, H. Fan, A. Zhang, W. Lai and W. Li, *Angew. Chem.*, 2025, **64**, e202501302.

81 H. Lu, H. Wang, G. Ran, S. Li, J. Zhang, Y. Liu, W. Zhang, X. Xu and Z. Bo, *Adv. Funct. Mater.*, 2022, **32**, 2203193.

82 X. Ran, Y. Shi, D. Qiu, J. Zhang, K. Lu and Z. Wei, *Nanoscale*, 2023, **15**, 18291–18299.

83 Q. Shen, C. He, B. Wu, Y. Lin, S. Chen, J. Gao, S. Li, Z. Ma, W. Ma, M. Shi, Y. Li and H. Chen, *Chem. Eng. J.*, 2023, **471**, 144472.

84 Y. Shi, J. Pan, J. Yu, J. Zhang, F. Gao, K. Lu and Z. Wei, *Sol. RRL*, 2021, **5**, 2100008.

85 X. Song, Y. Zhang, Y. Li, F. Li, X. Bao, D. Ding, M. Sun and R. Yang, *Macromolecules*, 2017, **50**, 6880–6887.

86 G. Xu, H. Rao, X. Liao, Y. Zhang, Y. Wang, Z. Xing, T. Hu, L. Tan, L. Chen and Y. Chen, *Chin. J. Chem.*, 2020, **38**, 1553–1559.

87 H. Ji, J. Li, M. Du, J. Yang, A. Tang, G. Li, Q. Guo and E. Zhou, *J. Phys. Chem. C*, 2021, **125**, 10876–10882.

88 J. Wang, P. Wang, T. Chen, W. Zhao, J. Wang, B. Lan, W. Feng, H. Liu, Y. Liu, X. Wan, G. Long, B. Kan and Y. Chen, *Angew. Chem.*, 2025, **64**, e202423562.

89 T. Wang, R. Sun, Y. Wu, W. Wang, M. Zhang and J. Min, *Chem. Mater.*, 2022, **34**, 9970–9981.

90 X. Wang, C. Xiao, X. Sun, A. Saparbaev, S. Lei, M. Zhang, T. Zhong, Z. Li, J. Zhang, M. Zhang, Y. Yu, B. Xiao, C. Yang and R. Yang, *Nano Energy*, 2022, **101**, 107538.

91 Q. Li, Y. Bai, S. Jiang, T. Zhang, X. Wang, Q. Li, L. Xue, Q. Yan and E. Zhou, *ACS Appl. Mater. Interfaces*, 2025, **17**, 9315–9321.

92 X. Kong, N. Yang, X. Zhang, J. Zhang, Z. Li, X. Li, Y. Wu, R. Sun, J. Li, A. Li, J. Min, G. Yang and C. Sun, *Energy Environ. Sci.*, 2025, **18**, 386–396.

93 J. Guo, S. Qin, J. Zhang, C. Zhu, X. Xia, Y. Gong, T. Liang, Y. Zeng, G. Han, H. Zhuo, Y. Li, L. Meng, Y. Yi, J. Chen, X. Li, B. Qiu and Y. Li, *Nat. Commun.*, 2025, **16**, 1503.

94 Z. Wang, S. Zhu, X. Peng, S. Luo, W. Liang, Z. Zhang, Y. Dou, G. Zhang, S. Chen, H. Hu and Y. Chen, *Angew. Chem.*, 2025, **64**, e202412903.

95 L. Xue, Y. Yang, J. Xu, C. Zhang, H. Bin, Z. G. Zhang, B. Qiu, X. Li, C. Sun, L. Gao, J. Yao, X. Chen, Y. Yang, M. Xiao and Y. Li, *Adv. Mater.*, 2017, **29**, 1703344.

96 J. Wu, F. Sun, X. Xia, L. R. Franco, Q. Chen, Y. Fu, R. B. Ribeiro, X. Lu, C. M. Araujo, X. Wang, R. Yang, X. Guo, D. Yu, M. Zhang and E. Wang, *Adv. Funct. Mater.*, 2025, **35**, 2423137.

97 M. Xie, Y. Shi, H. Zhang, J. Pan, J. Zhang, Z. Wei and K. Lu, *Chem. Commun.*, 2022, **58**, 4877–4880.

98 H. Chen, Y. Zou, H. Liang, T. He, X. Xu, Y. Zhang, Z. Ma, J. Wang, M. Zhang, Q. Li, C. Li, G. Long, X. Wan, Z. Yao and Y. Chen, *Sci. China: Chem.*, 2022, **65**, 1362–1373.

99 W. Zhang, K. Zhao, N. Zhang, Q. Dong, S. Shen, H. Lu, B. Hu, F. Zhao, S. Yuan, G. Lu, Y. Chen, Z. Ma, Z. Bo and J. Song, *Adv. Funct. Mater.*, 2025, **35**, 2423242.

100 Y. Ding, W. A. Memon, S. Xiong, S. Gong, M. Li, Z. Deng, H. Liu, Y. Liu, X. Chen, N. Zheng and F. He, *Adv. Mater.*, 2025, **37**, e2501671.

101 Y.-J. Xue, F.-Y. Cao, P.-K. Huang, Y.-C. Su and Y.-J. Cheng, *J. Mater. Chem. A*, 2020, **8**, 5315–5322.

102 H. Zhang, S. Li, B. Xu, H. Yao, B. Yang and J. Hou, *J. Mater. Chem. A*, 2016, **4**, 18043–18049.

103 Z. Zhang, Y. Li, G. Cai, Y. Zhang, X. Lu and Y. Lin, *J. Am. Chem. Soc.*, 2020, **142**, 18741–18745.

104 J. Zhu, A. Tang, L. Tang, P. Cong, C. Li, Q. Guo, Z. Wang, X. Xu, J. Wu and E. Zhou, *Chin. Chem. Lett.*, 2025, **36**, 110233.

105 J. Gao, N. Yu, Z. Chen, Y. Wei, C. Li, T. Liu, X. Gu, J. Zhang, Z. Wei, Z. Tang, X. Hao, F. Zhang, X. Zhang and H. Huang, *Adv. Sci.*, 2022, **9**, 2203606.

106 M. Jiang, H.-F. Zhi, B. Zhang, C. Yang, A. Mahmood, M. Zhang, H. Y. Woo, F. Zhang, J.-L. Wang and Q. An, *ACS Energy Lett.*, 2023, **8**, 1058–1067.

107 T. Xu, X. Zhang, S. Zhang, W. Zhang and W. Song, *ACS Appl. Mater. Interfaces*, 2024, **16**, 4618–4627.

108 Y. Zou, H. Chen, X. Bi, X. Xu, H. Wang, M. Lin, Z. Ma, M. Zhang, C. Li, X. Wan, G. Long, Y. Zhaoyang and Y. Chen, *Energy Environ. Sci.*, 2022, **15**, 3519–3533.

109 Y. Zou, Y. Dong, C. Sun, Y. Wu, H. Yang, C. Cui and Y. Li, *Chem. Mater.*, 2019, **31**, 4222–4227.

110 X. Duan, W. Song, J. Qiao, X. Li, Y. Cai, H. Wu, J. Zhang, X. Hao, Z. Tang, Z. Ge, F. Huang and Y. Sun, *Energy Environ. Sci.*, 2022, **15**, 1563–1572.

111 X. Chen, B. Kan, Y. Kan, M. Zhang, S. B. Jo, K. Gao, F. Lin, F. Liu, X. Peng, Y. Cao and A. K. Y. Jen, *Adv. Funct. Mater.*, 2020, **30**, 1909535.

112 P. Bi, S. Zhang, T. Xiao, M. Cui, Z. Chen, J. Ren, C. Qin, G. Lu, X. Hao and J. Hou, *Sci. China: Chem.*, 2021, **64**, 599–607.

113 L. Chen, J. Yi, R. Ma, L. Ding, T. A. Dela Pena, H. Liu, J. Chen, C. Zhang, C. Zhao, W. Lu, Q. Wei, B. Zhao, H. Hu, J. Wu, Z. Ma, X. Lu, M. Li, G. Zhang, G. Li and H. Yan, *Adv. Mater.*, 2023, **35**, 2301231.

114 Z. Chen, H. Yao, J. Wang, J. Zhang, T. Zhang, Z. Li, J. Qiao, S. Xiu, X. Hao and J. Hou, *Energy Environ. Sci.*, 2023, **16**, 2637–2645.

115 K. Chong, X. Xu, H. Meng, J. Xue, L. Yu, W. Ma and Q. Peng, *Adv. Mater.*, 2022, **34**, 2109516.

116 X. Cui, G. Ran, H. Lu, Y. Liu, H. Jiang, H. Zhang, D. Li, Y. Liu, Y. Lin, Z. Ma, W. Zhang, P. Cheng and Z. Bo, *Adv. Funct. Mater.*, 2024, **34**, 2400219.

117 Y. Cui, P. Zhu, H. Hu, X. Xia, X. Lu, S. Yu, H. Tempeld, R. A. Eichel, X. Liao and Y. Chen, *Angew. Chem.*, 2023, **62**, e202304931.

118 X. Du, Y. Yuan, L. Zhou, H. Lin, C. Zheng, J. Luo, Z. Chen, S. Tao and L. S. Liao, *Adv. Funct. Mater.*, 2020, **30**, 1909837.

119 H. Xiang, F. Sun, X. Zheng, B. Gao, P. Zhu, T. Cong, Y. Li, X. Wang and R. Yang, *Adv. Sci.*, 2024, **11**, 2401330.

120 H. Kang, Y. Jing, Y. Zhang, Y. Li, H. Zhang, H. Zhou and Y. Zhang, *Sol. RRL*, 2023, **7**, 2201084.

121 J. Ge, L. Hong, W. Song, L. Xie, J. Zhang, Z. Chen, K. Yu, R. Peng, X. Zhang and Z. Ge, *Adv. Energy Mater.*, 2021, **11**, 2100800.

122 Y. Han, H. Zhang, X. Xie, Z. Liu, K. Geng, Y. Yang, Y. Zhang and G. Chen, *Appl. Phys. A: Mater. Sci. Process.*, 2023, **129**, 122.

123 J. Pan, J. Guan, Z. Wang, R. Zhang, Y. Fu, X. Yu, Q. Zhang and Y. Han, *J. Mater. Chem. C*, 2024, **12**, 4142–4156.

124 H. Zhang, X. Wang, L. Yang, S. Zhang, Y. Zhang, C. He, W. Ma and J. Hou, *Adv. Mater.*, 2017, **29**, 1703777.

125 J. Hofinger, C. Putz, F. Mayr, K. Gugujonovic, D. Wielend and M. C. Scharber, *Mater. Adv.*, 2021, **2**, 4291–4302.

126 J. Zhao, J. Zhang, Y. Dou, K. Zhang, C. Zhu, Z. Zhong and F. Huang, *J. Mater. Chem. A*, 2024, **12**, 24862–24871.

127 S. Lai, Y. Cui, Z. Chen, X. Xia, P. Zhu, S. Shan, L. Hu, X. Lu, H. Zhu, X. Liao and Y. Chen, *Adv. Mater.*, 2024, **36**, 2313105.

128 K. E. Hung, Y. S. Lin, Y. J. Xue, H. R. Yang, Y. Y. Lai, J. W. Chang, C. J. Su, A. C. Su, C. S. Hsu, U. S. Jeng and Y. J. Cheng, *Adv. Energy Mater.*, 2022, **12**, 2103702.

129 B.-H. Jiang, Y.-S. Chen, Y.-C. You, Y.-W. Su, C.-Y. Chang, H.-S. Shih, Z.-E. Shi, C.-P. Chen and K.-T. Wong, *J. Mater. Chem. C*, 2024, **12**, 12004–12014.

130 H. Jiang, H. Lu, Z. Liang, Y. Li, G. Ran, C. Han, Y. Liu, H. Li, X. Bao and Z. Bo, *Sci. China: Chem.*, 2024, **67**, 3004–3011.

131 C. Li, X. Gu, Z. Chen, X. Han, N. Yu, Y. Wei, J. Gao, H. Chen, M. Zhang, A. Wang, J. Zhang, Z. Wei, Q. Peng, Z. Tang, X. Hao, X. Zhang and H. Huang, *J. Am. Chem. Soc.*, 2022, **144**, 14731–14739.

132 H. Liu, Z. Chen, R. Peng, Y. Qiu, J. Shi, J. Zhu, Y. Meng, Z. Tang, J. Zhang, F. Chen and Z. Ge, *Chem. Eng. J.*, 2023, **474**, 145807.

133 Q. Liu, S. Smeets, S. Mertens, Y. Xia, A. Valencia, J. D'Haen, W. Maes and K. Vandewal, *Joule*, 2021, **5**, 2365–2379.

134 J. Zhou, C. Guo, L. Wang, C. Chen, Z. Gan, Y. Sun, C. Liu, J. Zhou, Z. Chen, D. Gao, W. Xia, D. Liu, T. Wang and W. Li, *Nano Energy*, 2024, **129**, 109988.

135 Y. Li, J. Wu, X. Yi, Z. Liu, H. Liu, Y. Fu, J. Liu and Z. Xie, *J. Mater. Chem. C*, 2023, **11**, 13263–13273.

136 Z. Liu and N. Wang, *J. Mater. Chem. C*, 2019, **7**, 10039–10048.

137 Y. Wang, Y. Wang, L. Zhu, H. Liu, J. Fang, X. Guo, F. Liu, Z. Tang, M. Zhang and Y. Li, *Energy Environ. Sci.*, 2020, **13**, 1309–1317.

138 Z. Zhang, Q. Wu, D. Deng, S. Wu, R. Sun, J. Min, J. Zhang and Z. Wei, *J. Mater. Chem. C*, 2020, **8**, 15385–15392.

139 H. Jiang, H. Lu, Z. Liang, Y. Li, G. Ran, C. Han, Y. Liu, H. Li, X. Bao and Z. Bo, *Sci. China:Chem.*, 2024, **67**, 3004–3011.

140 Q. Liu, Y. Wang, J. Fang, H. Liu, L. Zhu, X. Guo, M. Gao, Z. Tang, L. Ye, F. Liu, M. Zhang and Y. Li, *Nano Energy*, 2021, **85**, 105963.

141 Y. Wei, Y. Cai, X. Gu, G. Yao, Z. Fu, Y. Zhu, J. Yang, J. Dai, J. Zhang, X. Zhang, X. Hao, G. Lu, Z. Tang, Q. Peng, C. Zhang and H. Huang, *Adv. Mater.*, 2023, **36**, 2304225.

142 Y. Qin, S. Zhang, Y. Xu, L. Ye, Y. Wu, J. Kong, B. Xu, H. Yao, H. Ade and J. Hou, *Adv. Energy Mater.*, 2019, **9**, 1901823.

143 D. Sun, Z. Chen, J. Zhang, W. Song, J. Shi, J. Zhu, Y. Meng, F. Jin, S. Yang and Z. Ge, *Sci. China: Chem.*, 2023, **67**, 963–972.

144 Y. Sun, C. Chen, L. Wang, C. Guo, J. Cai, D. Li, B. Zhou, C. Liu, D. Liu, T. Wang and W. Li, *ACS Mater. Lett.*, 2023, **5**, 1710–1717.

145 L. Cao, H. Zhang, X. Du, H. Lin, C. Zheng, G. Yang, M. Deng, X. Xu, S. Tao and Q. Peng, *Nano Energy*, 2024, **129**, 110016.

146 Y. Wang, B. Jia, J. Wang, P. Xue, Y. Xiao, T. Li, J. Wang, H. Lu, Z. Tang, X. Lu, F. Huang and X. Zhan, *Adv. Mater.*, 2020, **32**, 2002066.

147 D. H. Lee, D. H. Kim, T. Kim, D. C. Lee, S. Cho and T. Park, *Nano Energy*, 2022, **93**, 106878.

148 D. H. Lee, D. H. Kim, T. Kim, D. C. Lee, S. Cho and T. Park, *Nano Energy*, 2022, **93**, 106878.

149 H. Wang, Z. Zhang, J. Yu, P. C. Lin, C. C. Chueh, X. Liu, S. Guang, S. Qu and W. Tang, *ACS Appl. Mater. Interfaces*, 2020, **12**, 21633–21640.

150 J. Wang, Z. Zheng, P. Bi, Z. Chen, Y. Wang, X. Liu, S. Zhang, X. Hao, M. Zhang, Y. Li and J. Hou, *Natl. Sci. Rev.*, 2023, **10**, nwad085.

151 Y. Wang, K. Sun, C. Li, C. Zhao, C. Gao, L. Zhu, Q. Bai, C. Xie, P. You, J. Lv, X. Sun, H. Hu, Z. Wang, H. Hu, Z. Tang, B. He, M. Qiu, S. Li and G. Zhang, *Adv. Mater.*, 2024, **36**, 2411957.

152 Z. He, S. Li, R. Zeng, Y. Lin, Y. Zhang, Z. Hao, S. Zhang, F. Liu, Z. Tang and H. Zhong, *Adv. Mater.*, 2024, **36**, 2404824.

153 H. Bin, T. P. A. van der Pol, J. Li, B. T. van Gorkom, M. M. Wienk and R. A. J. Janssen, *Chem. Eng. J.*, 2022, **435**, 134878.

154 Y. Wang, Z. Liu, X. Cui, C. Wang, H. Lu, Y. Liu, Z. Fei, Z. Ma and Z. Bo, *J. Mater. Chem. A*, 2020, **8**, 12495–12501.

155 H. Xia, Y. Zhang, K. Liu, W. Deng, M. Zhu, H. Tan, P. W. K. Fong, H. Liu, X. Xia, M. Zhang, T. A. Dela Peña, R. Ma, M. Li, J. Wu, Y. Lang, J. Fu, W.-Y. Wong, X. Lu, W. Zhu and G. Li, *Energy Environ. Sci.*, 2023, **16**, 6078–6093.

156 J. Liu, H. Lu, Y. Yin, K. Wang, P. Wei, C. Song, Z. Miao and Q. Liang, *Battery Energy*, 2022, **1**, 20220013.

157 L. Zhan, S. Li, H. Zhang, F. Gao, T. K. Lau, X. Lu, D. Sun, P. Wang, M. Shi, C. Z. Li and H. Chen, *Adv. Sci.*, 2018, **5**, 1800755.

158 B. Kan, Y. Q. Q. Yi, X. Wan, H. Feng, X. Ke, Y. Wang, C. Li and Y. Chen, *Adv. Energy Mater.*, 2018, **8**, 1800424.

159 X. Liu, Z. He, H. Wang, K. Yang, Y. Zhang, Y. Zhang, Z. Geng, M. Duan, B. Tang, J. Xin, B. Qin, Q. Liang and J. Liu, *Adv. Funct. Mater.*, 2025, DOI: **10.1002/adfm.202517542**.

160 H. Hu, Z. Jin, J. Ge, C. Shen, L. Xie, W. Song, Q. Ye, P. Ding, J. Li, C. Han, X. Yu, Q. Liu and Z. Ge, *Adv. Mater.*, 2025, **37**, e2420308.

161 S. Yang, X. Huang, Y. Cho, S. Koo, Y. Ouyang, Z. Sun, S. Jeong, T. L. H. Mai, W. Kim, L. Zhong, S. Chen, C. Zhang, H. S. Lee, S. J. Yoon, L. Chen and C. Yang, *Angew. Chem.*, 2025, **64**, e202424287.

162 K. Shi, J. Lai, X. Xia, S. Jeong, C. Zhu, L. Zhou, J. Guo, J. Zhang, C. Yang, X. Li, L. Meng, Z. G. Zhang, B. Qiu and Y. Li, *Adv. Funct. Mater.*, 2024, **35**, 2411787.

163 T. Zhang, Y. Xu, X. Qu, Z. Chen, L. Ma, J. Wang, P. Bi, J. Dai, G. Wang, T. Zhang, J. Hou and H. Yao, *Macromolecules*, 2025, **58**, 9163–9170.

164 H. Tian, Y. Luo, Z. Chen, T. Xu, R. Ma, J. Wu, G. Li, C. Yang and Z. Luo, *Adv. Energy Mater.*, 2024, **15**, 2404537.

165 Z. Liu, Y. Fu, J. Wu, X. Yi, M. Zhao, M. Huang, J. Liu and Z. Xie, *Adv. Funct. Mater.*, 2024, **35**, 2401558.

166 H. B. Naveed, K. Zhou and W. Ma, *Acc. Chem. Res.*, 2019, **52**, 2904–2915.

167 G. Xie, Q. Xue, H. Ding, A. Liang, J. Liu, Y. Yang, J. Wang, X. Liao, Y. Min and Y. Chen, *Angew. Chem.*, 2025, **64**, e202504144.

168 C. Han, Z. Jin, C. Shen, M. Liu, W. Song, Q. Liu and Z. Ge, *Adv. Energy Mater.*, 2025, **15**, 2501682.

169 J. Zhang, J. Zhong, S. Chung, L. Bai, Z. Zhao, L. Tan, Y. Liu, M. Zhang, S. Lyu, J. Lee, L. Li, K. Cho and Z. Kan, *Chem. Eng. J.*, 2025, **522**, 167311.

170 Q. Xu, K. Xing, H. Zhu, J.-Y. Wang, D. Cai, D. Wang, K. Su, Y. Li, Y. Ma and Q. Zheng, *Sci. China: Chem.*, 2025, **68**, DOI: **10.1007/s11426-025-2745-0**.

171 Y. Xie, Y. Guo, P. C. Y. Chow, X. Tan, H. Xu, G. Lu, W. Ma and H. Yan, *Small*, 2025, e07273.

172 J. Xin, C. Zhao, Z. Geng, W. Xue, Z. Chen, C. Song, H. Yan, Q. Liang, Z. Miao, W. Ma and J. Liu, *Adv. Energy Mater.*, 2024, **14**, 2401433.

173 Q. Liang, H. Li, W. Xu, J. Lu, R. Ma, Q. Bai, X. Sun, M. Chen, L. Zhu, Q. Liu, Y. Guo, G. Zhang, Q. Xue, A. Iwan, P. Cheng, H. Hu, H. Wang, J. Chen, L. Niu and H. Sun, *Angew. Chem.*, 2025, **64**, e202425267.

174 L. Zhu, M. Zhang, G. Zhou, T. Hao, J. Xu, J. Wang, C. Qiu, N. Prine, J. Ali, W. Feng, X. Gu, Z. Ma, Z. Tang, H. Zhu, L. Ying, Y. Zhang and F. Liu, *Adv. Energy Mater.*, 2020, **10**, 1904234.

175 B. Zhang, W. Chen, J. Zhang, H. Mao, X. Gu, Z. Qin, D. Luo, L. Zhang and Y. Chen, *Sci. China: Chem.*, 2025, **68**, 2264–2273.